ARTICLE

Age and context of mid–Pliocene hominin cranium from Woranso–Mille, Ethiopia

Beverly Z. Saylor[1], Luis Gibert[2], Alan Deino[3], Mulugeta Alene[4], Naomi E. Levin[5], Stephanie M. Melillo[6], Mark D. Peaple[7], Sarah J. Feakins[7], Benjamin Bourel[8], Doris Barboni[8], Alice Novello[8], Florence Sylvestre[8], Stanley A. Mertzman[9] & Yohannes Haile–Selassie[10]*

A fossil hominin cranium was discovered in mid–Pliocene deltaic strata in the Godaya Valley of the northwestern Woranso–Mille study area in Ethiopia. Here we show that analyses of chemically correlated volcanic layers and the palaeomagnetic stratigraphy, combined with Bayesian modelling of dated tuffs, yield an age range of 3.804 ± 0.013 to 3.777 ± 0.014 million years old (mean $\pm 1\sigma$) for the deltaic strata and the fossils that they contain. We also document deposits of a perennial lake beneath the deltaic sequence. Mammalian fossils associated with the cranium represent taxa that were widespread at the time and data from botanical remains indicate that the vegetation in the lake and delta catchment was predominantly dry shrubland with varying proportions of grassland, wetland and riparian forest. In addition, we report high rates of sediment accumulation and depositional features that are typical of a steep topographic relief and differ from younger Woranso–Mille fossil localities, reflecting the influence of active rift processes on the palaeolandscape.

Until recently, field work in the Woranso-Mille area (Afar, Ethiopia) has concentrated on exposures along the Mille River that include more than 120 m of fossiliferous sedimentary and volcanic strata that are between 3.8 and 3.2 million years (Myr) old. East of Korsi Dora (Fig. 1a), sedimentary sequences that are younger than the extra-regional, approximately 3.57-Myr-old Kilaytoli tuff[1] have yielded specimens of at least 2 hominin species, *Australopithecus afarensis* and *Australopithecus deyiremeda*[2–5]. West of Korsi Dora, near the Waki-Mille confluence, volcanic and sedimentary layers between the approximately 3.76-Myr-old[1] Mille tuff sequence and the Kilaytoli tuff yielded dentognathic fossils that seem to be transitional between *A. anamensis* and *A. afarensis*[6]. A fossil cranium (MRD-VP-1/1), discovered in 2016 and reported in a companion paper[7], was recovered 6 km northwest of the Waki-Mille confluence in the Godaya Valley, where the section extends 55 m below the Mille tuff sequence and 60–125 m above it (Fig. 1b). The section below the Mille tuff sequence (Fig. 2) overlaps in age with the lowermost Hadar Formation[8–10] and the uppermost Sagantole Formation[11–13] of the neighbouring Awash Valley (Fig. 1a). Even though these formations are known for their Pliocene hominin fossils, they have yielded only a single hominin specimen between 4.1 and 3.6 Myr old[14,15]. Outside the Afar, the hominin record from this time interval is also limited[16–20].

Stratigraphic setting and age of the fossils

In the study area, the Godaya River passes between the high Guda plateau and the lower Miro Dora and Am-Ado plateaus (Fig. 1c). The low plateaus are covered by basalt flows that have been geochemically identified as the Am-Ado basalt group, one of six basalt groups in the Woranso-Mille area[21] (Supplementary Table 1). As these basalt groups are stratigraphically compact and chemically distinguishable, they form reliable chronostratigraphic markers (Fig. 1). The MRD-VP-1 fossil locality is at the bottom of the Miro Dora Plateau, around 23 m stratigraphically beneath the Am-Ado basalt group (Extended Data Fig. 1a).

The collection horizon consists of low outcrops of coarse sandstone, part of a succession of deltaic siltstone and sandstone (section S4 in Fig. 2, see 'Lake and delta sequence'). Most fossil specimens (including MRD-VP-1/1) show no sign of abrasion, although a few uncollected fragments have rolled edges, which is indicative of transport. The coarse sand matrix in the region of the orbits indicates MRD-VP-1/1 was buried in the coarse sandstone of the MRD-VP-1 locality (Extended Data Fig. 1b), although possibly after burial elsewhere had left a hard, fine-sand matrix in the nasal opening, cranial base and parts of the hard palate.

Tuffs above the Am-Ado basalt group are younger than the extra-regional approximately 3.66-Myr-old Waki tuff[22] based on stratigraphic and geochemical correlations to tuffs near the Waki-Mille confluence[22] (Extended Data Fig. 2 and Supplementary Table 2). These tuffs are preserved (1) northwest of MRD-VP-1, at and near the measured section S6; (2) southeast of MRD-VP-1 at Am-Ado; and (3) east of MRD-VP-1, along section S1, below the extra-regional, approximately 3.4-Myr-old[23] Sidi Hakoma tuff (Fig. 1).

Between the Am-Ado basalt group and the fossiliferous deltaic sequence is a tuffaceous interval (Fig. 1). This interval is thickest (around 22 m) at S2 (Lehaysule Gera hill; Extended Data Fig. 1c) where both the Am-Ado basalt flows and the sandstone of the deltaic sequence have pinched out. There it consists of metre-scale felsic pumice tuffs with interbedded basaltic pumice tuffs, scoria, pumice siltstone and siltstone, and includes the Mille tuff sequence, which is recognized on the basis of physical characteristics and stratigraphic position (Fig. 2). Tuffs below the Mille tuff sequence are typically devitrified; however, at S2 and S5 (3 km northwest of S2; Extended Data Fig. 1d) tuffs within and above the Mille tuff sequence yielded glass shards suitable for geochemical analysis (Supplementary Table 2). These tuffs are compositionally and stratigraphically similar to the Mille tuff sequence, 'bimodal tuff' (basaltic and rhyolitic) and Araskimiro tuff, which are closely associated tuffs near the Waki-Mille confluence that underlie

[1]Department of Earth, Environmental and Planetary Sciences, Case Western Reserve University, Cleveland, OH, USA. [2]Departament de Mineralogia, Petrologia i Geologia Aplicada Facultat de Ciències de la Terra, Universitat de Barcelona, Barcelona, Spain. [3]Berkeley Geochronology Center, Berkeley, CA, USA. [4]School of Earth Sciences, Addis Ababa University, Addis Ababa, Ethiopia. [5]Department of Earth and Environmental Sciences, University of Michigan, Ann Arbor, MI, USA. [6]Department of Human Evolution, Max Planck Institute for Evolutionary Anthropology, Leipzig, Germany. [7]Department of Earth Sciences, University of Southern California, Los Angeles, CA, USA. [8]Aix-Marseille University, CNRS, IRD, INRA, Collège de France, CEREGE, Aix-en-Provence, France. [9]Department of Earth and Environment, Franklin and Marshall College, Lancaster, PA, USA. [10]Cleveland Museum of Natural History, Cleveland, OH, USA. *e-mail: yhaileselassie@cmnh.org
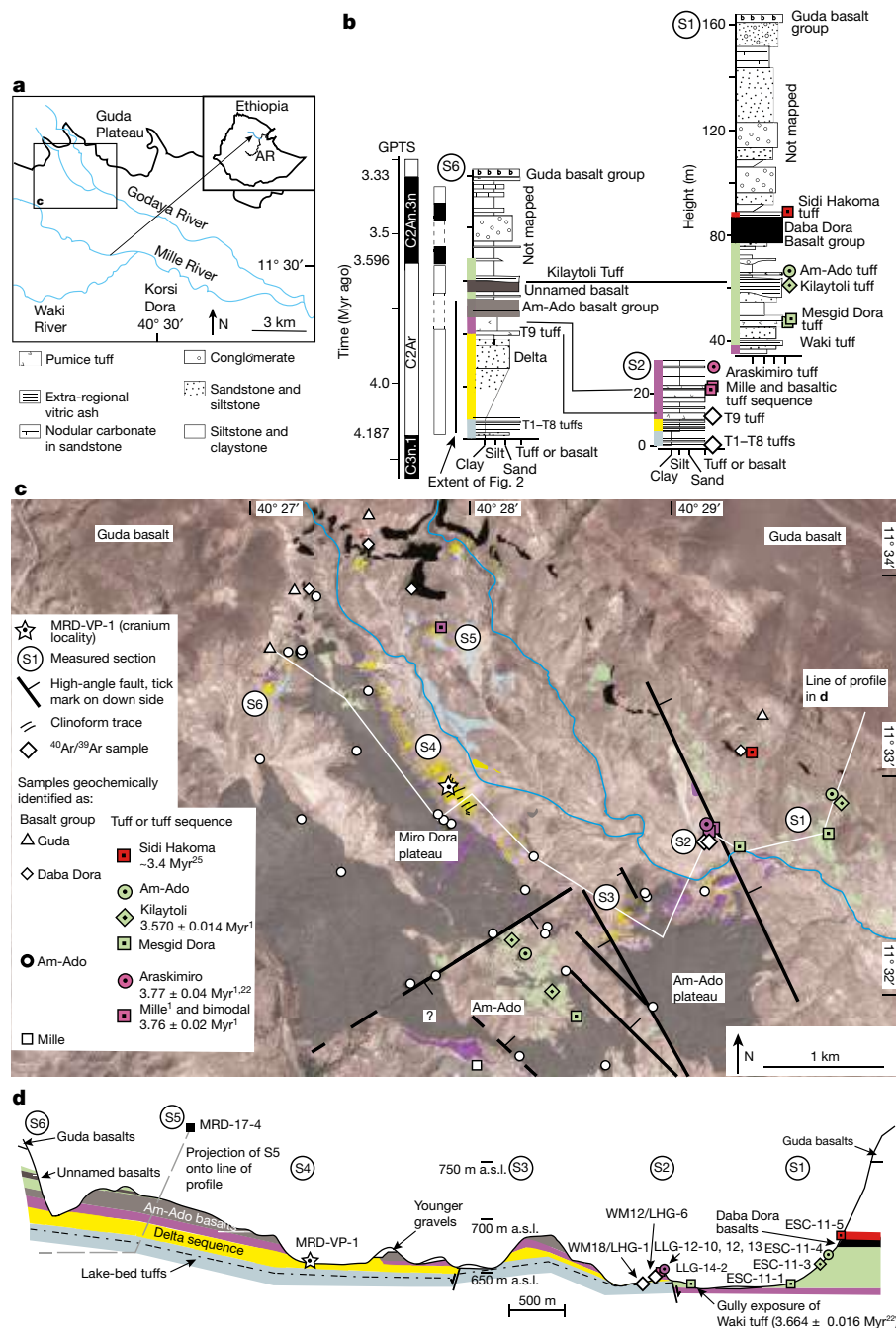
Fig. 1 | Stratigraphic setting of the fossil cranium. a, The location of the Godaya Valley relative to fossiliferous areas near the Waki-Mille confluence and east of Korsi Dora. AR, Awash River. **b–d**, Geological features of the Godaya Valley are illustrated as simplified stratigraphic columns (**b**), a partial geological map (**c**) and a cross-section along line of topographic profile with 10:1 vertical exaggeration (**d**). **b**, White and black rectangles next to section S6 indicate reverse and normal palaeomagnetic zones that correlate with the geopolarity time scale (GPTS)[24]. **c, d**, Ages

of tuff correlates are from previous studies[1,22,25]. **d**, Colours of mapped units are as in **b**; uncoloured areas are younger cover or not mapped; the documented stratigraphic offset is a criterion for fault identification in **c**. Note that changes in apparent dip in the cross-section correspond to changes in the orientation of the topographic profile. m a.s.l., metres above sea level. Supporting data are reported in Supplementary Tables 1–4. Data for the base map and topographic profile are from Google, DigitalGlobe.

the approximately 3.66-Myr-old Waki tuff and have statistically indistinguishable [40]Ar/[39]Ar ages[1,22] of 3.77–3.76 Myr (Fig. 1b and Extended Data Fig. 2). These geochemical correlations confirm the recognition of the Mille tuff sequence in the Godaya Valley, including across a north-westward facies change from fallout pumice tuffs in sections S2 and S3 to pumice siltstone in sections S4, S5 and S6 (Fig. 2). The age of the Mille tuff provides a minimum constraint[1] of around 3.76 Myr for the fossil horizon.

At the bottom of the tuffaceous interval is a coarse, locally thick (0–3 m) pumice lapillistone fallout tuff that is informally referred to

as T9 (Fig. 2). T9 is underlain by deltaic sediments, below which there is lacustrine claystone with thin (mostly less than 10 cm) intercalated tuffs. These lakebed tuffs are best exposed at S2 and S6 where the lithologic characteristics, spacing and uniformity of thickness permit bed-for-bed correlations (tuff units T1–T8) across more than 4 km (Extended Data Fig. 3). Thus, although the T1–T8 tuffs are not exposed at S4, they can confidently be projected below the fossil horizon there (Figs. 1d, 2). Two tuffs from S2 were dated using the [40]Ar/[39]Ar laser incremental-heating dating method, providing bracketing constraints on the age of the delta sequence. These are WM12/LHG-6, a sample of
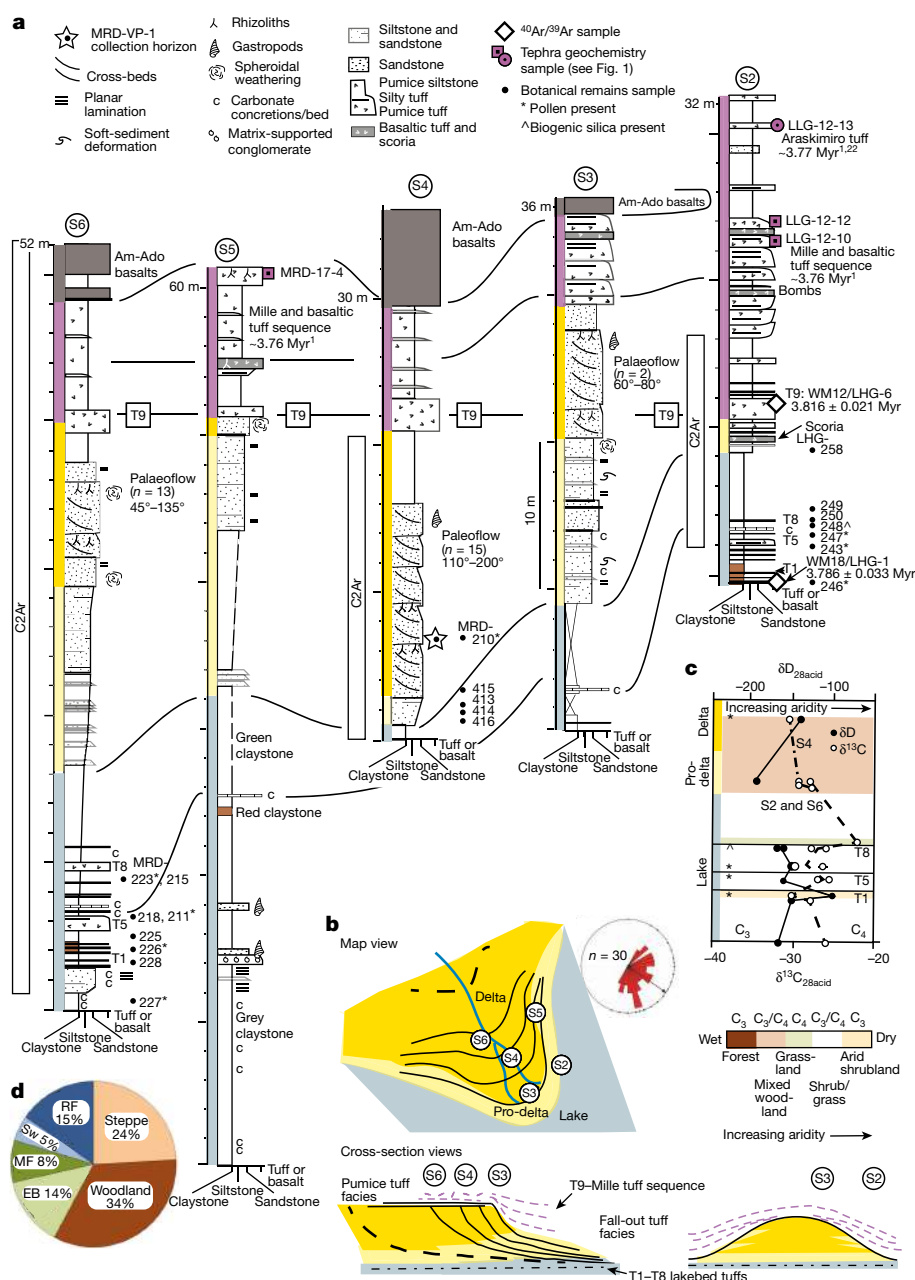
Fig. 2 | Lake, delta and tuffaceous strata below and above the level where the hominin cranium was found. a, Measured stratigraphic sections below the Am-Ado basalt group hung on the dated T9 tuff. **b**, Cartoon illustrating the southeastward progradation of the delta front (thick black lines) over the lake bed tuffs (T1–T8) and the subsequent partial infill of topography on top of the delta by overlying tuffaceous strata (T9–Mille tuff sequence). Rose diagram shows palaeocurrent directions measured on trough axes and foreset dips in the deltaic sandstone. **c**, Stable hydrogen and carbon isotope data from *n*-alkanoic

acids in claystone, siltstone and sandstone samples (*n* = 16) plotted in their relative stratigraphic positions. Error bars based on the s.d. of instrument duplicates are smaller than the size of the symbols, with the exception of the $\delta^{13}C$ value above T5. **d**, Habitat scores for sample WM18-MRD-210 calculated based on the percentage of pollen taxa with affinity for each habitat[35]. EB, evergreen bushland; MF, montane forest; RF, riparian forest; Sw, swamp. Supporting data are reported in Supplementary Tables 2–10.

the T9 tuff, and WM18/LHG-1, a sample of a 2-cm-thick tuff, 30 cm below T1 (Fig. 2, section S2).

The $^{40}Ar/^{39}Ar$ dating experiments involved single-crystal laser incremental heating of individual phenocrysts. In total, 10 out of 13 incremental-heating experiments from WM12/LHG-6 and all 8 experiments from WM18/LHG-1 yielded apparent-age plateaus (Extended Data Fig. 4 and Supplementary Table 3). The argon isotope data from the plateau steps were plotted on inverse-isochron $^{36}Ar/^{40}Ar$ and $^{39}Ar/^{40}Ar$ correlation diagrams (Extended Data Fig. 5), the results of which are displayed as age–probability density spectra in Extended Data Fig. 6, combining all individual crystal isochron results for each

sample into a single population. The weighted-mean age of the quasi-symmetrical, quasi-Gaussian modes representing the two populations is 3.816 ± 0.021 Myr old for WM12/LHG-6 (1σ including the error in *J*, the neutron-fluence parameter; mean square weighted deviation (MSWD) = 1.46) and 3.786 ± 0.033 Myr old for WM18/LHG-1 (MSWD = 0.07). Although apparently inverted (the lower sample age is younger than the higher), the ages are indistinguishable given the large uncertainties due to low K abundance in plagioclase for WM12/LHG-6 and small grain size (around 200–400 μm) for WM18/LHG-1. These results are consistent with an age[1] of around 3.76 Myr old for the Mille tuff sequence (Fig. 2).

We computed a Bayesian stratigraphic age model for section S2 that extends from the lowermost dated tuff (WM18/LHG-1) to the Mille tuff sequence, as well as a similar model for the laterally equivalent but thicker interval at S6 (Extended Data Fig. 2). These models allow interpolation of ages for the bottom (3.804 ± 0.013 Myr at S2 and 3.802 ± 0.016 Myr at S6) and top (3.798 ± 0.014 Myr at S2 and 3.777 ± 0.014 Myr at S6) of the deltaic sediments, which yielded indistinguishable estimates and an age range of 3.804 ± 0.013 Myr to 3.777 ± 0.014 Myr for the deltaic sediments and the cranium.

Palaeomagnetic reversal stratigraphy supports this age assignment. A 100-m reverse–normal–reverse palaeomagnetic sequence at S6 includes a more than 64 m-thick reverse zone at the bottom that extends from 46 m below to 18 m above the Am-Ado basalt group, encompassing the T1–T9 tuffs and the Mille tuff sequence (Fig. 1, Extended Data Fig. 7 and Supplementary Table 4). This zone is correlated with palaeomagnetic subchron C2Ar (which is 4.187–3.596 Myr old)[24]. Its lower boundary is not locally exposed, but its upper boundary with the normal C2An.3n (3.596–3.33 Myr old)[24] is identified 5 m above the Kilaytoli tuff, consistent with the position of this subchron boundary at Korsi Dora[1,25]. Reverse palaeomagnetic strata at S2 and S4 are consistent with the correlation of these sections with C2Ar (Fig. 2 and Extended Data Fig. 7). On the basis of the modelled ages of tuffs, the sediment accumulation rate for the interval between WM18/LHG-1 and the Mille tuff sequence is 320 m per Myr at S2 and 820 m per Myr at S6 (Supplementary Table 5). These high rates contrast with lower accumulation rates above the Mille tuff sequence at S6 (90–100 m per Myr for intervals up to the top of the C2An.3n normal zone) and S2 (170–210 m per Myr for intervals up to the Sidi Hakoma tuff).

Lake and delta sequence

The sedimentary interval below the T9 tuff is 10.5 m (S2) to 51.5 m (S5) thick and consists of three facies: claystone, heterolithic interbeds and coarse-to-pebbly sandstone (Fig. 2). The claystone facies exceeds 32 m at S5, the lower part of which is greenish grey with carbonate concretions and beds of conglomerate, gastropods and sandstone. The conglomerate is matrix-supported and, along the drainage between S4 and S5, in beds up to 2 m thick with sand-filled root casts (Fig. 1). Clasts are sub-rounded, up to 15 cm across and diverse, including basalt, rhyolite, quartzite, sandstone and reworked carbonate nodules. The upper part of the claystone is greyish green and locally red, and contains the altered lakebed tuffs (WM18/LHG-1, T1–T8; Fig. 2). Claystone grades upward into 2–14 m of sandier upward, heterolithic interbeds. Decimetre-scale sandstone beds within this facies have sharp bases, normal grading and soft-sediment deformation. Above the heterolithic facies is 0–13 m of coarse-to-pebbly sandstone; this is the facies that contained MRD-VP-1/1. At S3, S4 and S6, this sandstone is tabular and trough cross-bedded and planar-stratified. Straight-crested foresets are 3–5.5 m high and, at MRD-VP-1 (S4), are traceable in satellite images, which reveal dominantly southeast to southwest palaeoflow directions (Fig. 1c and Extended Data Fig. 1e). Field measurements of palaeoflow directions range from northeast to southwest (Fig. 2).

Claystone is a product of slow settling in a lake environment, beyond the normal reach of coarser sediment, whereas the matrix-supported conglomerate is characteristic of debris flows, which can transport material for long distances even on shallow slopes or under water[26]. However, root casts in the conglomerate and an absence of clay in overlying gastropod sandstone indicate that these beds were associated with lake-margin settings that were subject to plant colonization and winnowing of fine sediment. By contrast, the lateral continuity of the lakebed tuffs (T1–T8) in the upper part of the claystone facies is consistent with suspension fallout on the floor of a perennial lake without evidence of winnowing, erosion or desiccation. The large, straight-crested foresets in the sandstone are typical of clinoforms that are formed by a Gilbert-type delta in which a river enters a lake and rapidly deposits its coarse sediment load[27]. Trough cross-bedding and planar stratification associated with, and above, the clinoforms are consistent with fluvial top sets (Fig. 2). Sedimentary structures in the

heterolithic facies are typical of current- or density-generated flows, which occur in pro-delta and lake-margin settings, in front of and next to delta lobes[27]. The complex stratigraphy includes multi-leveled cross-sets that may reflect internal delta dynamics or repeated episodes of progradation, yet it is clear that before the T9 tuff, the delta had built southeastward above the T1–T8 tuffs to at least as far as MRD-VP-1 (S4), and that before the Mille tuff, a lobe had reached S3 (Extended Data Fig. 1f). From there, the deltaic sandstone thins northeastward towards S2, pinching out over approximately 1 km. Changes in lobe thickness and depositional settings along and across the delta axis can account for changes in the overlying tuffaceous interval. In this scenario, fallout tuffs at S2 and S3 accumulated above the sloping delta front, partially filling the surface relief, and pumice siltstone at S4, S5 and S6 accumulated on the flatter surface behind the delta front, where the tephra was more completely reworked and mixed with silt by the fluvial system that fed and cut across the top of the delta (Fig. 2b).

Associated fauna and palaeoecological context

Only 26 vertebrate specimens have been collected from MRD-VP-1 to date. They sample a variety of mammalian taxa (Supplementary Table 6), most of which are common in other eastern African hominin-bearing sites of comparable age, but do not allow conclusive palaeoenvironmental inferences. Still, the sedimentary facies at MRD-VP-1, together with botanical remains separated from the lake and delta sediments (see below), suggest habitats that are associated with the margins of a lake, a delta and the riparian zone upstream.

The $\delta^{13}C_{28acid}$ values of n-alkanoic acids derived from plant wax and pollen markers for Somalia-Masai shrubland/grassland (Poaceae, Amaranthaceae, *Indigofera* and Capparidaceae) in the same sediment samples indicate that the catchment for this basin was dry C_3-dominated shrubland with some C_4 vegetation (Fig. 2c and Supplementary Tables 7–9). Only one sample was consistent with C_4 grass dominance ($\delta^{13}C_{28acid} = -22.0‰$). Pollen abundances were insufficient for rigorous plant community analysis except for one sample, WM18-MRD-210, from the deltaic sandstone of MRD-VP-1 ($n = 222$). For this sample, the habitat scores are highest for steppe (25%) and woodland (3%) habitats (Fig. 2d). On the basis of the high proportions of *Acacia*, Poaceae and *Aerva*-type *javanica* in this sample (Extended Data Figs. 8, 9), we conclude that the catchment area for the delta was typical of dry, open *Acacia* woodland. The relatively high habitat scores for riparian forest (15%) and evergreen bushland (14%) types suggest that such environments were present upstream of, and close to, the hominin site. This sample (WM18-MRD-210) from the hominin-bearing sediment of MRD-VP-1 also yielded the lowest $\delta^{13}C_{28acid}$ values ($-30.6‰$) consistent with a greater proportion of C_3 trees, wetter or more closed canopy. We note that mature palaeosols with distinct horizons are not present in the lacustrine or deltaic strata, consistent with the high rates of sediment accumulation and short exposure times for any land surfaces.

The evidence from the botanical proxies is broadly consistent with the wind-blown and regionally averaged signals recorded in marine sediments in the Gulf of Aden, for which the catchment area includes the Afar[28]. Specifically, the $\delta^{13}C_{28acid}$ (-30.6 to $-22.0‰$; $n = 15$) and δD_{28acid} (-100 to $-198‰$; $n = 10$) values from the plant wax we studied encompass the spatially averaged $\delta^{13}C_{wax}$ (-28.9 to $-24.7‰$; $n = 75$) and δD_{wax} (-146 to $-132‰$; $n = 6$) results for the corresponding interval of a Gulf of Aden marine core[29]. Pollen from this core interval reveal that modern-analogue assemblages, including variations in 10–50% Amaranthaceae and 9–30% grass[30], were prevalent regionally at this time, which indicates that the wetter conditions represented by the lake and delta sediments were local to this setting rather than products of a wet climatic interval.

The lake was at least 9 km^2 (based on exposures) and at least 6–8 m deep (based on clinoform heights). Alteration of volcanic glass combined with poor preservation of biogenic silica suggests alkaline conditions. In addition, LHG-248—the only sample to yield identifiable silica remains (Extended Data Fig. 9)—is composed of 17 diatom

species (10 genera), most of which are indicators of saline environments, predominantly (70%) those observed in coastal and marine environments (Supplementary Table 10). Furthermore, pink pigmentation in the lipid extract of some sediment samples is consistent with carotenoids in saline lakes[31]. The lake probably had a closed outlet at times. Diverse conglomerate clasts could have been derived from underlying Oligocene and Miocene basalts and rhyolites that were tilted steeply on west–southwest-dipping normal faults before approximately 4 Myr ago[32] (Extended Data Fig. 10). However, Afromontane taxa (*Hagenia abyssinica*) that today occur in the upper limit of the mountain forest[33] above 2,450 m are evidence that the catchment area of the lake included the Ethiopian highlands (Supplementary Table 9). This low-dispersal pollen may have been delivered by a river that—similar to the modern Mille River—descended the western margin of the Afar and turned southeastward around the palaeolandscape (Extended Data Fig. 10). The Gilbert-style delta and debris flows are features that are typical of high topographic relief and, together with the high sediment accumulation rates, are compatible with rapid filling of the space that was created by the crustal thinning[32] more than 4 Myr ago or by syn-depositional faulting. Although we have identified no faults that were demonstrably active during the time of the lake and delta, high-angle faults that offset the mapped strata and the eastward thickening of strata from S6 to S1 are evidence of continued tectonic activity. More work is needed to determine whether, and how, lake deposits in the Godaya Valley relate to the ≥3.8-Myr-old lake deposits elsewhere, especially along the Mille and Waki rivers, in southwestern Woranso-Mille and in the Awash Valley (Extended Data Fig. 10). Although lakes are common in rift basins, it is notable that similar lake and Gilbert-type delta deposits of this age have not been documented elsewhere in the Afar. In general, the thick lacustrine strata of the Godaya Valley are not predicted by models of the Hadar Basin as an east-dipping half-graben, which place the thickest, deepest deposits near inferred bounding fault(s) that are more than 40 km to the southeast, but are compatible with models of basin formation associated with rift-axis volcanic centres related to the Red Sea Rift[9,12,34]. In either case, the decreased sediment accumulation rate and increased alluvial conglomerate above the Mille tuff sequence and Sidi Hakoma tuff, respectively (Fig. 1b), indicate changes in basin dynamics and the landscape between the setting of the 3.80-Myr-old MRD-VP-1/1 hominin and younger fossils that have been recovered at other Woranso-Mille localities[2–6].

Online content

Any methods, additional references, Nature Research reporting summaries, source data, extended data, supplementary information, acknowledgements, peer review information; details of author contributions and competing interests; and statements of data and code availability are available at https://doi.org/10.1038/s41586-019-1514-7.

1. Deino, A. L. et al. ⁴⁰Ar/³⁹Ar dating, paleomagnetism, and tephrochemistry of Pliocene strata of the hominid-bearing Woranso-Mille area, west-central Afar Rift, Ethiopia. *J. Hum. Evol.* **58**, 111–126 (2010).
2. Haile-Selassie, Y. et al. An early *Australopithecus afarensis* postcranium from Woranso-Mille, Ethiopia. *Proc. Natl Acad. Sci. USA* **107**, 12121–12126 (2010).
3. Haile-Selassie, Y. et al. A new hominin foot from Ethiopia shows multiple Pliocene bipedal adaptations. *Nature* **483**, 565–569 (2012).
4. Haile-Selassie, Y. et al. New species from Ethiopia further expands Middle Pliocene hominin diversity. *Nature* **521**, 483–488 (2015).
5. Haile-Selassie, Y. et al. Dentognathic remains of *Australopithecus afarensis* from Nefuraytu (Woranso-Mille, Ethiopia): comparative description, geology, and paleoecological context. *J. Hum. Evol.* **100**, 35–53 (2016).
6. Haile-Selassie, Y., Saylor, B. Z., Deino, A., Alene, M. & Latimer, B. M. New hominid fossils from Woranso-Mille (Central Afar, Ethiopia) and taxonomy of early *Australopithecus. Am. J. Phys. Anthropol.* **141**, 406–417 (2010).
7. Haile-Selassie, Y. et al. A 3.8-million-year-old hominin cranium from Woranso-Mille, Ethiopia. *Nature* https://doi.org/10.1038/s41586-019-1513-8 (2019).
8. Taieb, M., Johanson, D. C., Coppens, Y. & Aronson, J. L. Geological and palaeontological background of Hadar hominid site, Afar, Ethiopia. *Nature* **260**, 289–293 (1976).
9. Campisano, C. J. & Feibel, C. S. in *The Geology of Early Humans in the Horn of Africa* Vol. 446 (eds Quade, J. &Wynn, J.) 179–201 (Geological Society of America, 2008).
10. Wynn, J. G. et al. in *The Geology of Early Humans in the Horn of Africa* Vol. 446 (eds Quade, J. & Wynn, J.) 87–118 (Geological Society of America, 2008).
11. Renne, P. R., WoldeGabriel, G., Hart, W. K., Heiken, G. & White, T. D. Chronostratigraphy of the Miocene–Pliocene Sagantole Formation, Middle Awash Valley, Afar rift, Ethiopia. *Geol. Soc. Am. Bull.* **111**, 869–885 (1999).
12. White, T. D. et al. Asa Issie, Aramis and the origin of *Australopithecus. Nature* **440**, 883–889 (2006).
13. Quade, J. et al. in *The Geology of Early Humans in the Horn of Africa* Vol. 446 (eds Quade, J. & Wynn, J.) 1–31 (Geological Society of America, 2008).
14. Asfaw, B. The Belohdelie frontal: new evidence of early hominid cranial morphology from the Afar of Ethiopia. *J. Hum. Evol.* **16**, 611–624 (1987).
15. White, T. D. et al. New discoveries of *Australopithecus* at Maka in Ethiopia. *Nature* **366**, 261–265 (1993).
16. Leakey, M. G., Feibel, C. S., McDougall, I. & Walker, A. New four-million-year-old hominid species from Kanapoi and Allia Bay, Kenya. *Nature* **376**, 565–571 (1995).
17. Leakey, M. G., Feibel, C. S., McDougall, I., Ward, C. & Walker, A. New specimens and confirmation of an early age for *Australopithecus anamensis. Nature* **393**, 62–66 (1998).
18. Deino, A. in *Paleontology and Geology of Laetoli: Human Evolution in Context* Vol. 1 (ed. Harrison, T.) 77–97 (Springer, 2011).
19. Fleagle, J. G., Rasmussen, D. T., Yirga, S., Bown, T. M. & Grine, F. E. New hominid fossils from Fejej, southern Ethiopia. *J. Hum. Evol.* **21**, 145–152 (1991).
20. Kappelman, J. et al. Age of *Australopithecus afarensis* from Fejej, Ethiopia. *J. Hum. Evol.* **30**, 139–146 (1996).
21. Alene, M. et al. Geochemistry of Woranso-Mille Pliocene basalts from west-central Afar, Ethiopia: implications for mantle source characteristics and rift evolution. *Lithos* **282–283**, 187–200 (2017).
22. Saylor, B. Z. et al. Tephrostratigraphy of the Waki-Mille area of the Woranso-Mille paleoanthropological research project, Afar, Ethiopia. *J. Hum. Evol.* **93**, 25–45 (2016).
23. Walter, R. C. & Aronson, J. L. Age and source of the Sidi Hakoma Tuff, Hadar Formation, Ethiopia. *J. Hum. Evol.* **25**, 229–240 (1993).
24. Lourens, L., Hilgen, F., Laskar, J. & Wilson, D. S. in *A Geological Time Scale* (eds Gradstein, F. M. et al.) 409–440 (Cambridge Univ. Press, 2004).
25. Saylor, B. Z. et al. in *The Postcranial Anatomy of* Australopithecus afarensis (eds Haile-Selassie, Y. & Su, D.) 13–23 (Springer, 2016).
26. Middleton, G. V. & Hampton, M. A. in *Marine Sediment Transport and Environmental Management* Ch. 11 (eds Stanley, D. J. & Swift, P.) 197–218 (Wiley, 1976).
27. Elliot, T. in *Sedimentary Environments and Facies* (ed. Reading, H. G.) 113–154 (Blackwell Scientific, 1986).
28. Prospero, J. M. et al. Environmental characterization of global sources of atmospheric soil dust identified with the NIMBUS 7 Total Ozone Mapping Spectrometer (TOMS) absorbing aerosol product. *Rev. Geophys.* **40**, 1002 (2002).
29. Liddy, H. M., Feakins, S. J. & Tierney, J. E. Cooling and drying in northeast Africa across the Pliocene. *Earth Planet. Sci. Lett.* **449**, 430–438 (2016).
30. Bonnefille, R. Cenozoic vegetation, climate changes and hominid evolution in tropical Africa. *Global Planet. Change* **72**, 390–411 (2010).
31. Winters, Y. D., Lowenstein, T. K. & Timofeeff, M. N. Identification of carotenoids in ancient salt from Death Valley, Saline Valley, and Searles Lake, California, using laser Raman spectroscopy. *Astrobiology* **13**, 1065–1080 (2013).
32. Stab, M. et al. Modes of rifting in magma-rich settings: tsectono-magmatic evolution of Central Afar. *Tectonics* **35**, 2–38 (2016).
33. Friis, I., Demissew, S. & van Breugel, P. *Atlas of the Potential Vegetation of Ethiopia* (The Royal Danish Academy of Sciences and Letters, 2010).
34. Lahitte, P., Gillot, P. Y. & Courtillot, V. Silicic central volcanoes as precursors to rift propagation: the Afar case. *Earth Planet. Sci. Lett.* **207**, 103–116 (2003).
35. Prentice, I. C., Guiot, J., Huntley, B., Jolly, D., & Cheddadi, R. Reconstructing biomes from palaeoecological data: a general method and its application to European pollen data at 0 and 6 ka. *Clim. Dyn.* **12**, 185–194 (1996).

METHODS

Basalt geochemistry. Powdered basalt samples were analysed for major and trace element concentration using a PANalytical 2404 X-ray fluorescence vacuum spectrometer at Franklin and Marshall College, following previously described techniques[36]. This includes determination of ferrous iron by standard titration methods and total volatile content by loss on ignition. Samples were assigned to chronostratigraphically distinct basalt groups based on the similarity of element concentrations and stratigraphic position to previously characterized basalt groups[21] (Supplementary Table 1).

Tephra geochemistry. Tuff samples were prepared for glass geochemical analysis as previously described[22]. Elemental concentrations in felsic volcanic glass were measured in polished mounts using wavelength dispersive spectroscopy at the University of Wisconsin on Cameca SX-51 and Cameca SX-Five Fe electron probe micro-analysers. The mounts were carbon-coated at the same time as standards, which included Kilbourne olivine for magnesium, Minas Gerais rutile for titanium, Monash andesine for calcium, synthetic manganese olivine for manganese, Rockport fayalite for iron, topaz for fluorine, USMN chlorapatite for chlorine and Lipari obsidian for silicon, aluminium, oxygen, sodium and potassium. Analyses were conducted using an accelerating voltage of 15 KeV, a beam current of 10 nA, and a focused beam with onpeak and offpeak count times of 20 s. Element concentrations were converted to oxides computing all iron as Fe_2O_3, corrected for beam-induced ion migration of NaO, oxygen and K_2O using time-dependent intensity data, and normalized for differences in water content. Analyses with totals less than 97.5 or greater than 102.5 were excluded, except for MRD-17-4, for which analyses with water-adjusted totals less than 89.5 were excluded. The normalized oxide composition was compared with chemically characterized tuffs near the Waki-Mille confluence[22] (Supplementary Table 2).

$^{40}Ar/^{39}Ar$ dating. Two fallout tuff horizons were analysed using the single-crystal $^{40}Ar/^{39}Ar$ laser incremental-heating dating method. These samples were collected in stratigraphic sequence at Lahaysule Gera hill (S2); sample WM18/LHG-1 is from a 2-cm-thick medium-to-fine-grained tuff (30 cm below tuff unit T0) at the base of the exposures in the lacustrine sequence that underlies the area, while WM12/LHG-6 was obtained around 2 m above the base of a prominent, approximately 3 m thick, coarsely crystalline white lapillistone tuff (unit T9) above the lacustrine beds as well as deltaic siltstone. Following standard mineral purification procedures, WM18/LHG-1 yielded K-feldspar phenocrysts for analysis (approximately 0.2–0.4-mm grain size), whereas WM12/LHG-6 lacked K-feldspar but yielded plagioclase samples (around 0.45–1.5 mm) that were suitable for analysis. The plagioclase separate from WM12/LHG-6 was irradiated for 0.5 h in the Cd-lined in-core CLICIT facility of the Oregon State University TRIGA reactor. Two laboratory identifiers were assigned to this material (26236 and 26238), representing near-adjacent aliquot positions around the ring of a single aluminium irradiation sample holder. K-feldspar from WM18/LHG-1 was irradiated in the same facility for 10 h. Both irradiations used sanidine phenocrysts from the Alder Creek Rhyolite of California as the monitor mineral (age = 1.1848 ± 0.006 Myr)[37]. Reactor-induced isotopic production ratios for this irradiation were: $(^{36}Ar/^{37}Ar)_{Ca}$ = 2.65 ± 0.02 × 10^{-4}, $(^{38}Ar/^{37}Ar)_{Ca}$ = 1.96 ± 0.08 × 10^{-5}, $(^{39}Ar/^{37}Ar)_{Ca}$ = 6.95 ± 0.09 × 10^{-4}, $(^{37}Ar/^{39}Ar)_{K}$ = 2.24 ± 0.16 × 10^{-4}, $(^{38}Ar/^{39}Ar)_{K}$ = 1.220 ± 0.003 × 10^{-2}, $(^{40}Ar/^{39}Ar)_{K}$ = 2.5 ± 0.9 × 10^{-4}. Atmospheric values $(^{40}Ar/^{36}Ar$ = 298.56 ± 0.31) were obtained from a previous study[38] and decay constants have previously been published[39].

Following irradiation, phenocrysts were analysed individually (n = 13 for WM12/LHG-6; n = 21 for WM18/LHG-1) under ultra-high vacuum using a CO_2 laser with top-hat beam profile at a diameter of 2.3 mm. Argon analyses were executed on-line with the extraction system, using a five-detector Nu Instruments Noblesse mass spectrometer operating in ion-counting, simultaneous collection mode. All grains of WM12/LHG-6 were analysed incrementally from a very low degas temperature to fusion in six steps (Extended Data Fig. 4 and Supplementary Table 3). However, in the case of WM18/LHG-1, each grain was analysed in one or two low-power steps to allow a preliminary assessment of age and chemistry; grains that were too old (more than 10 Myr old, n = 12) or exhibited a Ca/K ratio of plagioclase (n = 1) were omitted, leaving 8 grains taken to completion of the incremental heating sequence. Further details of irradiation procedure, argon analysis and data reduction are provided in a previously published study[24].

Palaeomagnetic stratigraphy. Three main areas were selected, measured and sampled to analyse the magnetostratigraphy. A stratigraphic section that included the lowest and highest outcropping strata in the local area was produced for each of these three areas, which are (from west to east): Guda plateau (S6), the area around MRD-VP-1 (S4), and Lehaysule Gera hill (S2), northeast of the Am-Ado plateau. The longest section (S6) is a composite of two sections measured on both sides of a gully. Section S4 extends from the lowest strata below the fossiliferous sandstones to the top of the Miro Dora plateau, including tuffs and sediments above the Am-Ado basalts in the northwestern portion of the plateau. In total, 33 samples were collected and analysed from these areas: 24 at S6 (part a and b),

5 at S4 and 4 at S2. Samples were collected from fresh outcrops after digging and removing weathered superficial material. Mainly fine-grained sediments (clay and silt) were selected for sampling. Block samples of approximately 500 cm^3 were cut using manual tools and one flat face was oriented using a Brunton compass. In the laboratory, each sample was sawed, sanded and cleaned with compressed air and separated into at least 3 cubic specimens (10.5 cm^3). Measurements were done with a 2G three-axis cryogenic magnetometer at the University of Barcelona/CSIC palaeomagnetic laboratory. At least 2 specimens from each sample (a total of 79 specimens) were thermally demagnetized in a non-inductive furnace (less than 10 nT), at 50-°C steps up to 650 °C to remove secondary magnetizations and to isolate the primary characteristic magnetic direction. Magnetic susceptibility was measured with a KLY02 susceptibility bridge (Agico) at each demagnetization step to monitor possible mineralogical changes during the heating process.

Samples, in general, are of good quality and most show non-ambiguous palaeomagnetic directions with all specimens from each sample, showing consistent normal or reverse directions. In a limited number of specimens, the secondary magnetization was not completely removed showing ambiguous directions. The magnetic susceptibility was measured after each thermal demagnetization step, primarily to monitor mineralogical changes that might occur during heating. Samples show high magnetic susceptibility and no important changes are shown until the sample was heated to high temperatures of more than 500 °C. Overall, the samples yielded unblocking temperatures of more than 600 °C, indicating that magnetite was the main carrier of the magnetization. Palaeomagnetic directions were calculated using principal component analysis with the Paldir software (Extended Data Fig. 7 and Supplementary Table 4).

In general, samples show a low temperature component of the magnetization that was removed after heating at 250–300 °C, allowing isolation of a primary high-temperature component. In some specimens, the secondary component of the magnetization was not completely removed after demagnetization, and the resulting remanent directions are a mixture of normal and reverse polarities. These specimens show ambiguous directions, such as declinations towards the south, but positive inclinations or declinations towards the north with a negative inclination. We note also that sample MRD17 shows evidence of weathering with formation of new iron-rich minerals and a suspicious normal magnetization between two reverse samples. The 58 non-ambiguous specimens were selected to calculate mean normal and reverse characteristic remanent magnetizations and build a local polarity sequence correlated with the geopolarity time scale[24] based on available $^{40}Ar/^{39}Ar$ dates (Extended Data Fig. 7).

Leaf wax extraction and isotopic analysis. Sediment samples including claystone (n = 8), siltstone (n = 7) and sandstone (n = 1) were analysed for leaf-wax compound-specific isotopes (Supplementary Tables 7, 8). Samples were fragmented with a hammer before powdering with a ring and puck mill. Lipids were extracted using a Dionex Accelerated Solvent system with 9:1 dichloromethane (DCM):methanol at 100 °C and 1,500 psi. The total lipid extract was separated into neutral and acid fractions over NH_2 sepra bulk packing, the neutral fraction was eluted using 2:1 DCM:isopropanol and the acid fraction was eluted with 4% formic acid in diethyl ether. The acid fraction was methylated in a mixture of 95:5 methanol:hydrochloric acid at 70 °C for 12 h, using methanol of known isotopic composition ($\delta^{13}C$ = −24.7‰ and δD = −187‰). Excess Milli-Q water was added and the fatty acid methyl esters (FAMEs) were partitioned into hexane, dried by passing through anhydrous Na_2SO_4 and purified over a silica gel column and eluted with DCM. Unsaturated compounds were removed from samples by passing over a silver-nitrate-treated silica gel column, eluting the saturated FAMEs with DCM.

n-Alkanoic acids were identified using an Agilent 6890 gas chromatograph equipped with an Rxi-5ms (30 m × 0.25 mm, film thickness 0.25 μm) column connected to a 5973 MSD mass spectrometer, and quantified using the flame ionization detector. Samples were dissolved in 500 μl of hexane and 1 μl of this solution was injected into the inlet using a 7683 programmable autosampler. Quantification of FAMEs was conducted through comparison of sample peak areas in chromatograms to peak areas of an in-house standard containing known concentrations of n-alkanoic acids.

Carbon and hydrogen isotopes of n-alkanoic acids were measured using a Thermo Scientific Trace gas chromatograph equipped with a Rxi-5ms column (30 m × 0.25 mm; film thickness, 1 μm) with a PTV injector operated in solvent-split mode, coupled to a Delta V Plus isotope ratio mass spectrometer using an Isolink combustion/pyrolysis furnace (1,000/1,420 °C). A standard of known isotopic compositions (A6 mix supplied by A. Schimmelmann, University of Indiana) was measured daily, allowing for normalization to the Vienna Standard Mean Ocean Water/Standard Light Antarctic Precipitation and Vienna Pee Dee Belemnite/Lithium carbonate standard prepared by L. Svec isotopic scales for δD and $\delta^{13}C$ values, respectively. The root mean square error of the replicate analyses of the external standard was 4‰ for δD and 0.1‰ for $\delta^{13}C$. Sample $\delta^{13}C$ and δD values were corrected using a mass balance for the addition of the methyl group of known isotopic composition, as previously described[40].

Pollen extraction and analysis. We prepared 16 samples—most of which were the same as those analysed for leaf wax isotopes and phytoliths (Supplementary Table 7)—for microscopic pollen analysis following a standard procedure: (1) samples (5–30 g, depending on the sediment that was available) were immersed in HCl (33%, 1 h) to remove carbonates; (2) digestion of silicate minerals in HF (48%, 12 h); (3) immersion in HCl (33%, 4 h) to remove fluorosilicates produced in the previous step; (4) immersion in KOH (20%, 10 min in a hot water bath) to remove organic matter; (5) sieving at 150 µm; (6) heavy liquid separation using sodium polytungstate set at a specific gravity of 2.2 grams per cm^3 to improve pollen concentration. For productive samples, the entire residue sample was analysed under a microscope. Slides were prepared with glycerin and sealed with Entellan. They were scanned at a magnification of ×250 and identified at a magnification of ×1,000.

Pollen identifications (Supplementary Table 9) are based on the pollen reference collection available at CEREGE, Aix-en-Provence and published pollen atlases. Palaeovegetation inferences are based on modern pollen studies from east as well as west Africa[4], botanical surveys, interpretations proposed earlier by R. Bonnefille for Hadar and Middle Awash[30,41,42], and unpublished modern pollen data of B.B. from the Afar region Supplementary Table 9. For the MRD-210 pollen assemblage, habitat scores were calculated on the basis of pollen taxa diversity and pollen percentages following the biomization procedure[35]. This method allows a given taxon to be assigned to different habitats. Pollen percentages are square-rooted to reduce the weight of overrepresented taxa. The greater the number of taxa contributing to a given habitat and the higher their relative abundances (as a percentage), the higher the score of the given habitat is. Consequently, habitat types with higher scores can be considered closer (because these are best represented in terms of taxa diversity and abundance) than those with lower scores. Poaceae were excluded from score calculation to improve the signal.

Biogenic silica extraction and analysis. The same 16 samples that were analysed for leaf wax isotopes were also processed for phytoliths, using a process modified from a previous study[43]. The processing was done on approximately 1 g of the original material for each sample. Hydrochloric acid and nitric acid (heated) steps were, respectively, used to remove the carbonates and oxidize the organic matter. They were alternated with two sieving steps combined with numerous rounds of centrifugation to first remove the largest mineral fraction (≥ 250 µm), and then the smallest fraction, which included clays. Finally, a densimetric separation of the biogenic silica fraction using a zinc bromide heavy liquid set at a $d = 2.3$ was performed. Residues were obtained in minor amounts for all samples. Owing to their scarcity, samples were all mounted on slides using Canada balsam medium and observed at ×1,000 magnification. Sample WM18-MRD-210 is the only exception with abundant residues; however, these were mostly volcanic ash particles rather than biogenic silica. WM18-LHG-248, the only sample to yield identifiable taxa (including diatoms), was reprocessed with 2–3 g of material to enable species identification (Supplementary Table 10).

Reporting summary. Further information on research design is available in the Nature Research Reporting Summary linked to this paper.

Data availability

Any data supporting the findings of this study that are not included in the paper and Supplementary Information are available from the corresponding author upon reasonable request.

Code availability

A data analysis version of the $^{40}Ar/^{39}Ar$ dating software is available at no cost from A.D. (adeino@bgc.org). The Bayesian age–stratigraphic analysis model is available at https://github.com/brenhinkeller.

36. Mertzman, S. A. K–Ar results from the southern Oregon-northern California Cascade range. *Or. Geol.* **62**, 99–122 (2000).
37. Niespolo, E. M., Rutte, D., Deino, A. L. & Renne, P. R. Intercalibration and age of the Alder Creek sanidine $^{40}Ar/^{39}Ar$ standard. *Quat. Geochronol.* **39**, 205–213 (2017).
38. Lee, J.-Y. A redetermination of the isotopic abundances of atmospheric Ar. *Geochim. Cosmochim. Acta* **70**, 4507–4512 (2006).
39. Min, K. W., Mundil, R., Renne, P. R. & Ludwig, K. R. A test for systematic errors in $^{40}Ar/^{39}Ar$-geochronology through comparison with U/Pb analysis of a 1.1-Ga rhyolite. *Geochim. Cosmochim. Acta* **64**, 73–98 (2000).
40. Lee, H. et al. Comparison of three methods for the methylation of aliphatic and aromatic compounds. *Rapid Commun. Mass Spectrom.* **31**, 1633–1640 (2017).
41. Bonnefille, R., Vincens, A. & Buchet, A. Palynology, stratigraphy and palaeoenvironment of a Pliocene hominid site (2.9–3.3 M.Y.) at Hadar, Ethiopia. *Palaeogeogr. Palaeoclimatol. Palaeoecol.* **60**, 249–281 (1987).
42. Bonnefille, R., Potts, R., Chalié, F., Jolly, D. & Peyron, O. High-resolution vegetation and climate change associated with Pliocene *Australopithecus afarensis*. *Proc. Natl Acad. Sci. USA* **101**, 12125–12129 (2004).
43. Strömberg, C. A. E. The Origin and Spread of Grass-Dominated Ecosystems during the Tertiary of North America and How It Relates to the Evolution of Hypsodonty in Equids. PhD Thesis, Univ. California Berkeley (2003).
44. Deino, A. L. et al. Chronostratigraphic model of a high-resolution drill core record of the past million years from the Koora Basin, south Kenya Rift: overcoming the difficulties of variable sedimentation rate and hiatuses. *Quat. Sci. Rev.* **215**, 213–231 (2019).
45. Miall, A.D. *The Geology of Fluvial Deposits: Sedimentary Facies, Basin Analysis and Petroleum Geology* (Springer, 1996).
46. DiMaggio, E. N. et al. Late Pliocene fossiliferous sedimentary record and the environmental context of early *Homo* from Afar, Ethiopia. *Science* **347**, 1355–1359 (2015).
47. Kirschvink, J. L. The least-squares line and plane and the analysis of palaeomagnetic data. *Geophys. J. Int.* **62**, 699–718 (1980).
48. Sournia, A. *Diatomées planctoniques du Canal de Mozambique et de l'Île de la Réunion* (ORSTOM, 1968).
49. Foged, N. *Some Littoral Diatoms from the Coast of Tanzania* (Biblioteca Phycologia, 1975).
50. Ryan, W. B. F. et al. Global multi-resolution topography synthesis. *Geochem. Geophys. Geosyst.* **10**, Q03014 (2009).

Author contributions B.Z.S., L.G., M.A., A.D., N.E.L., S.M.M., M.D.P. and Y.H.-S. conducted field research. M.A. analysed basalt samples and S.A.M. analysed the samples for major and trace element concentrations. B.Z.S. collected and analysed tuff samples for major and minor element abundances in glass. A.D. collected and analysed tuff samples for $^{40}Ar/^{39}Ar$ dating. L.G. collected sediment samples and analysed their palaeomagnetic polarity. N.E.L. and M.D.P. collected sediment samples for analysis of botanical remains. S.M.M. contributed to the collection and analysis of mammalian fossils. M.D.P. and S.J.F. analysed and interpreted leaf wax isotopes. B.B. and D.B. separated and identified pollen. A.N. and F.S. separated and identified phytolith and diatom components. Y.H.-S. collected and analysed the mammalian fossils and directed the field station. B.Z.S. took the lead in writing the paper with contributions from all co-authors.
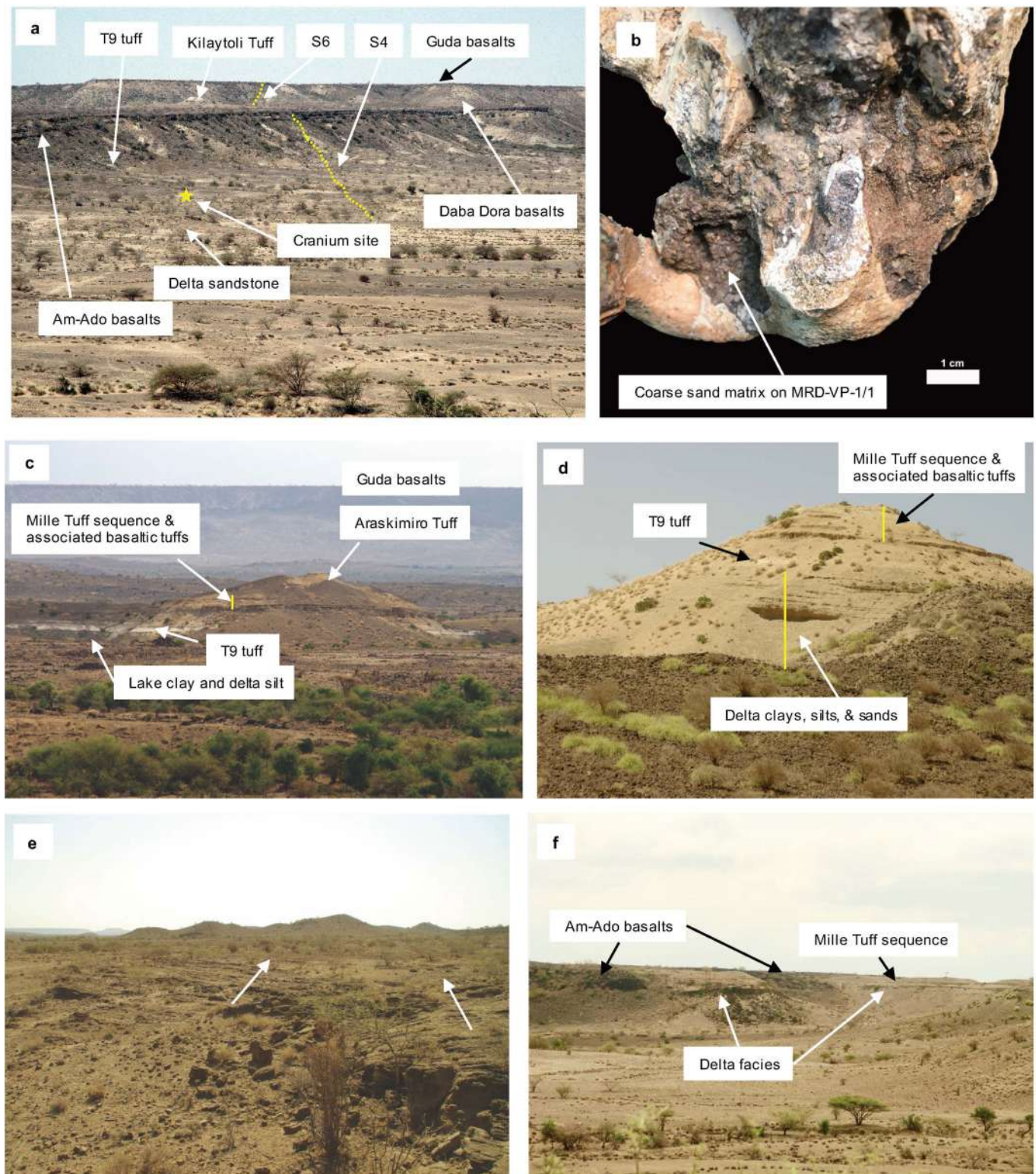
Extended Data Fig. 1 | Field photographs. a, Location of the horizon of the MRD-VP-1 fossil relative to features on the Miro Dora plateau (capped by Am-Ado basalts) and the higher Guda plateau (background). **b,** Coarse sand matrix on MRD-VP-1/1. Additional matrix types, which are not shown, included very hard fine sand and soft silty clay. **c,** Lehaysule Gera hill (section S2); image shows the position of geochemically identified tuffs (Mille tuff sequence and associated basaltic tuffs, and Araskimiro tuff) and the dated T9 tuff (WM12/LHG-6) above dark deltaic siltstone and lacustrine claystone. A lower dated tuff (WM18/LHG-1) near the bottom of the claystone exposure is not discernable. **d,** The hill of section S5; image shows the position of the deltaic sequence relative to the geochemically identified Mille tuff and associated basaltic tuff sequence and T9 tuff. **e,** Large-scale cross-bedded sandstone at MRD-VP-1. Arrows show foreset dip directions, indicating the flow toward the southeast (right arrow) and toward the south-southwest (left arrow). **f,** Upward-coarsening delta lobe(s) along the Am-Ado Plateau (S3) with Mille tuff sequence and Am-Ado basalt above and between.
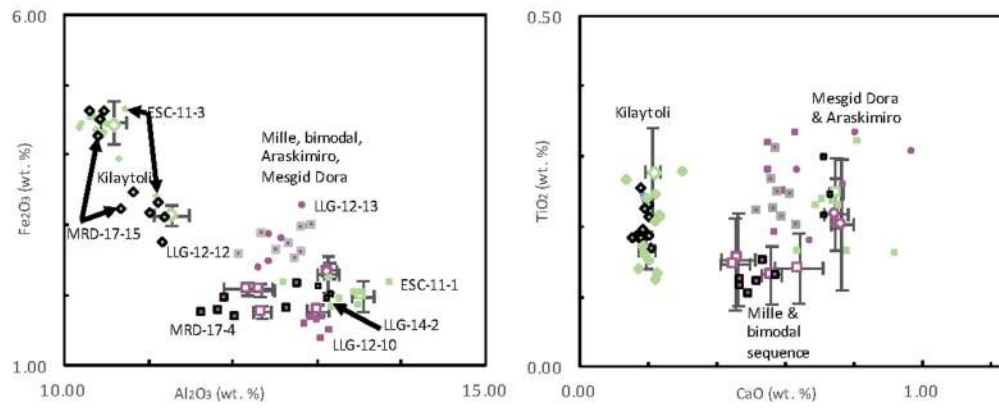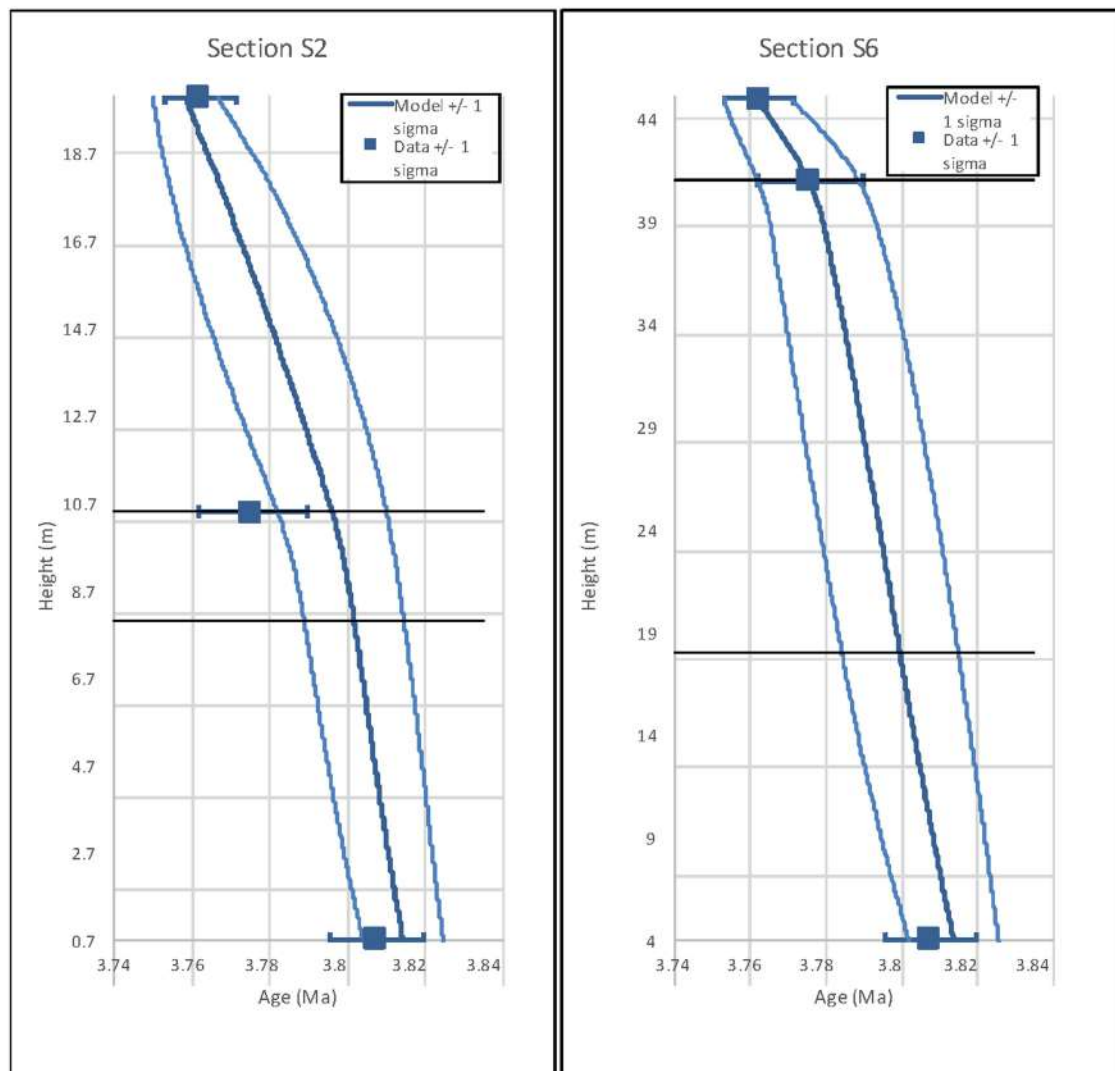
Extended Data Fig. 2 | See next page for caption.

Extended Data Fig. 2 | Tephrochemical data and age–depth models.
a, Bivariate plots of oxide abundances in volcanic glass normalized for
differences in water content (Supplementary Table 2). Symbol colours
and shapes are as in Fig. 1 with closed, smaller symbols indicating newly
reported analyses of individual glass shards from samples from the study
area, differentiated by symbol border colour and size. Open symbols indicate
previously published[22] sample means with 1σ variation for named tuffs
near the Waki-Mille confluence, specifically: Kilaytoli tuff (WM-KSD-3,
$n = 19$, 11 high iron and 8 low iron), Mesgid Dora tuff (MSD-08-5, $n = 12$),
Araskimiro tuff (MSD-08-3R, $n = 12$ and WM-MD5 P, $n = 10$, duplicate
samples from same location), bimodal tuff (WMC-08-3, $n = 16$, $n = 10$,
duplicate analyses of same sample), Mille tuff sequence (ARI-08-3, $n = 16$,
ARI-08-4, $n = 11$, two chemically similar, vertically adjacent tuffs in the

sequence). The Mille tuff sequence, the rhyolitic component of the basaltic
and rhyolitic 'bimodal tuff' and their correlates are distinguished from other
pumice tuffs in the area by their low CaO abundances. The Araskimiro
tuff and its correlates are distinguished from chemically similar pumice
tuffs in the area, including the Mesgid Dora tuff, by position above the
Mille tuff/basaltic tuff sequence and below the Waki tuff, which is present
below the Mesgid Dora tuff in a drainage approximately 300 m to the east
of S2 (Fig. 1d). **b**, Bayesian age–stratigraphic model[44] for $n = 3$ tuffs at S2,
including the lowermost dated tuff (WM18/LHG-1), the T9 tuff (WM12/
LHG-6) and the bottom of the Mille tuff sequence (around 2 m below LLG-
12-10, which is chemically similar to the Mille/basaltic tuff sequence), and a
similar model correlating these horizons to S6.
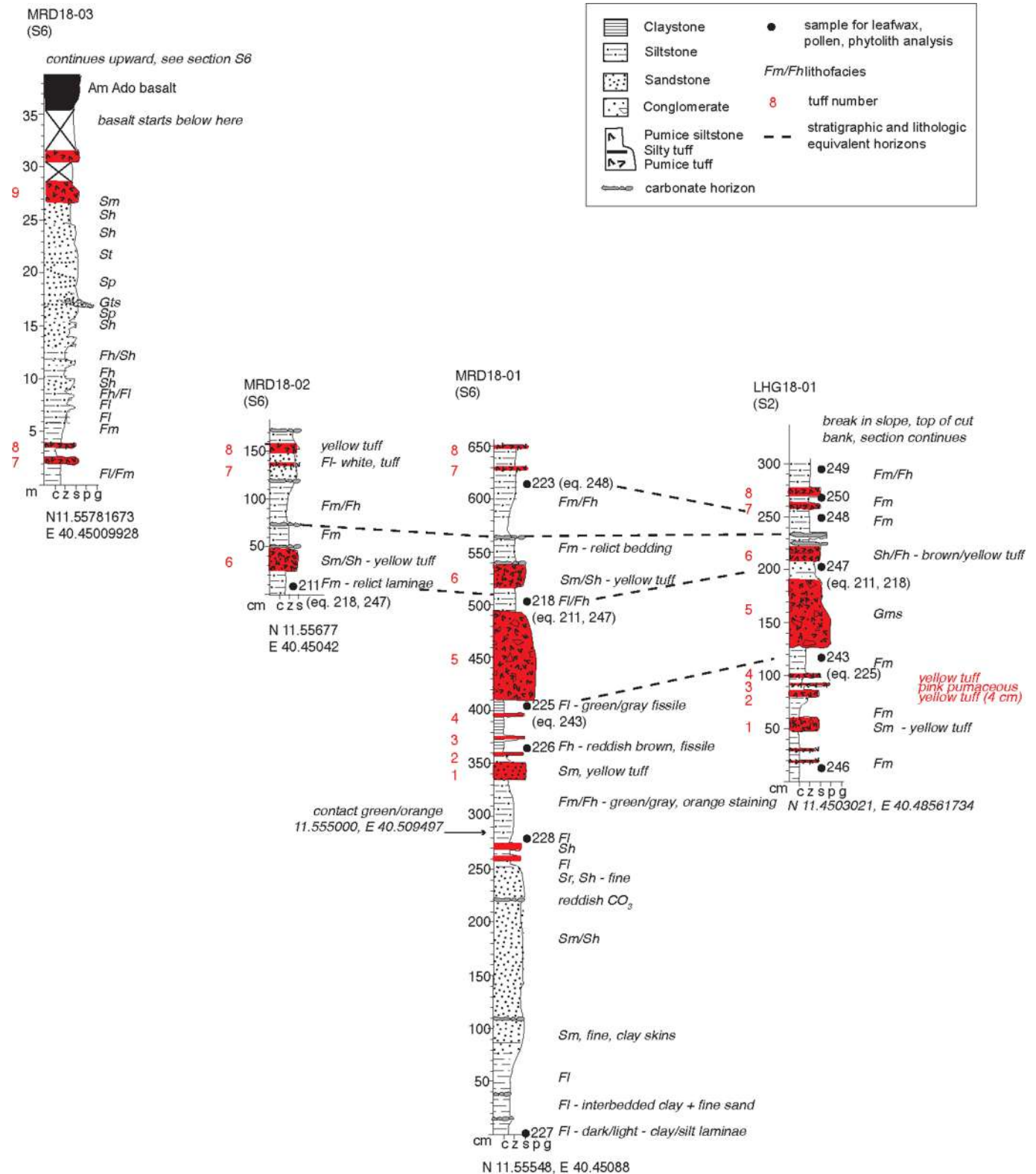
Extended Data Fig. 3 | Detailed stratigraphic sections with positions of samples that were investigated and analysed for leaf wax, pollen and phytolith content. All sections are in centimetres except for MRD18-03. Names of sections are listed at the top of each column and equivalent section names reported in Fig. 2 are listed in parentheses. The number associated with each sample identifier is listed next to the dot that indicates the stratigraphic position of samples. If sample numbers are equivalent stratigraphically to other samples, this is noted in parentheses. Tuff numbering is included on the left of each column. Dashed lines provide ties between stratigraphic and lithologic equivalent horizons

for non-tuffaceous units. The tuff numbering scheme also indicates tie points. Facies classification abbreviations are from a previously published study[45]. F, S and G indicate grain size (clay or silt size, sand size and gravel size, respectively) and the descriptors m, h, l, p and t describe the primary bedding as massive, horizontal, laminated, planar and trough, respectively. Listed latitudes and longitudes are in reference to the WGS-84 datum and indicate the position of the base of the section unless otherwise noted. The stratigraphic positions for samples WM18-MRD-210, -413, -414, -416 (section S4) and WM18-LHG-258 (section S2) can be found in Fig. 2.
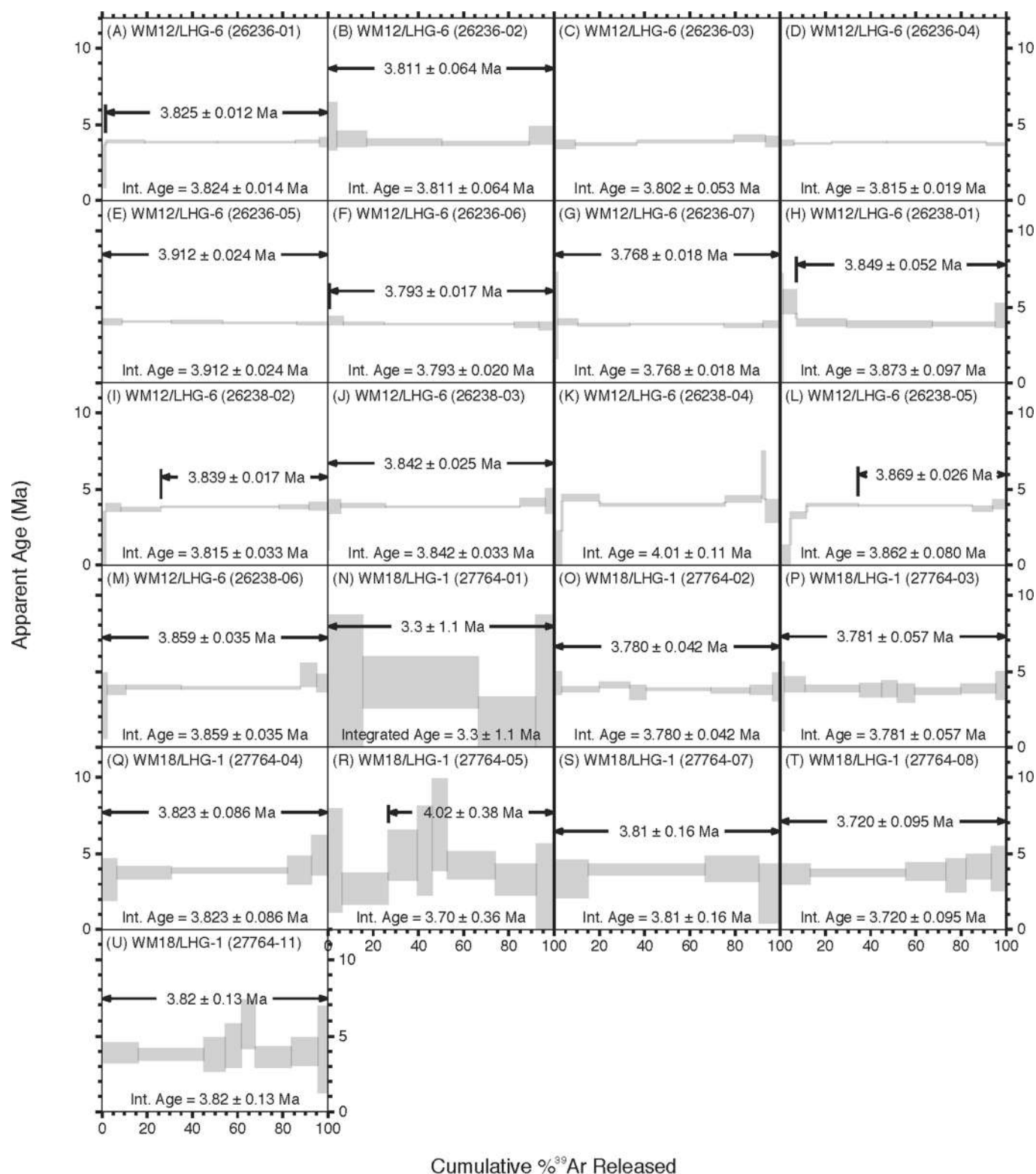
Extended Data Fig. 4 | Incremental heating release spectra from single-grain ^{40}**Ar/**^{39}**Ar analyses.** The x axis of each subplot is the cumulative percentage release of ^{39}Ar during the course of the experiment. 'Int. Age' is the 'integrated' or total-gas age, obtained by isotopically summing the individual steps weighted by the inverse variance, with the error calculated as the modified standard error at 1σ (standard error of the weighted mean multiplied by the square root of the MSWD when MSWD > 1). The apparent age plateau—defined as a sequence of at least three or more consecutive steps representing at least half of the total ^{39}Ar release, and for which analytical error alone is sufficient to explain the observed age dispersion at a probability of 95%—is calculated as the mean age weighted by the inverse variance, with the error shown as the 1σ modified standard error. Neither the integrated age nor plateau age incorporated the error in J at this stage in the data reduction; this systematic error is included in the final weighted-mean age calculated from the isochron results. Results for sample WM12/LHG-6 indicated n = 10 plateaus identified out of a total of n = 13 single-crystal incremental heating experiments; for sample WM18/LHG-1, n = 8 plateaus were found in n = 8 heating experiments.
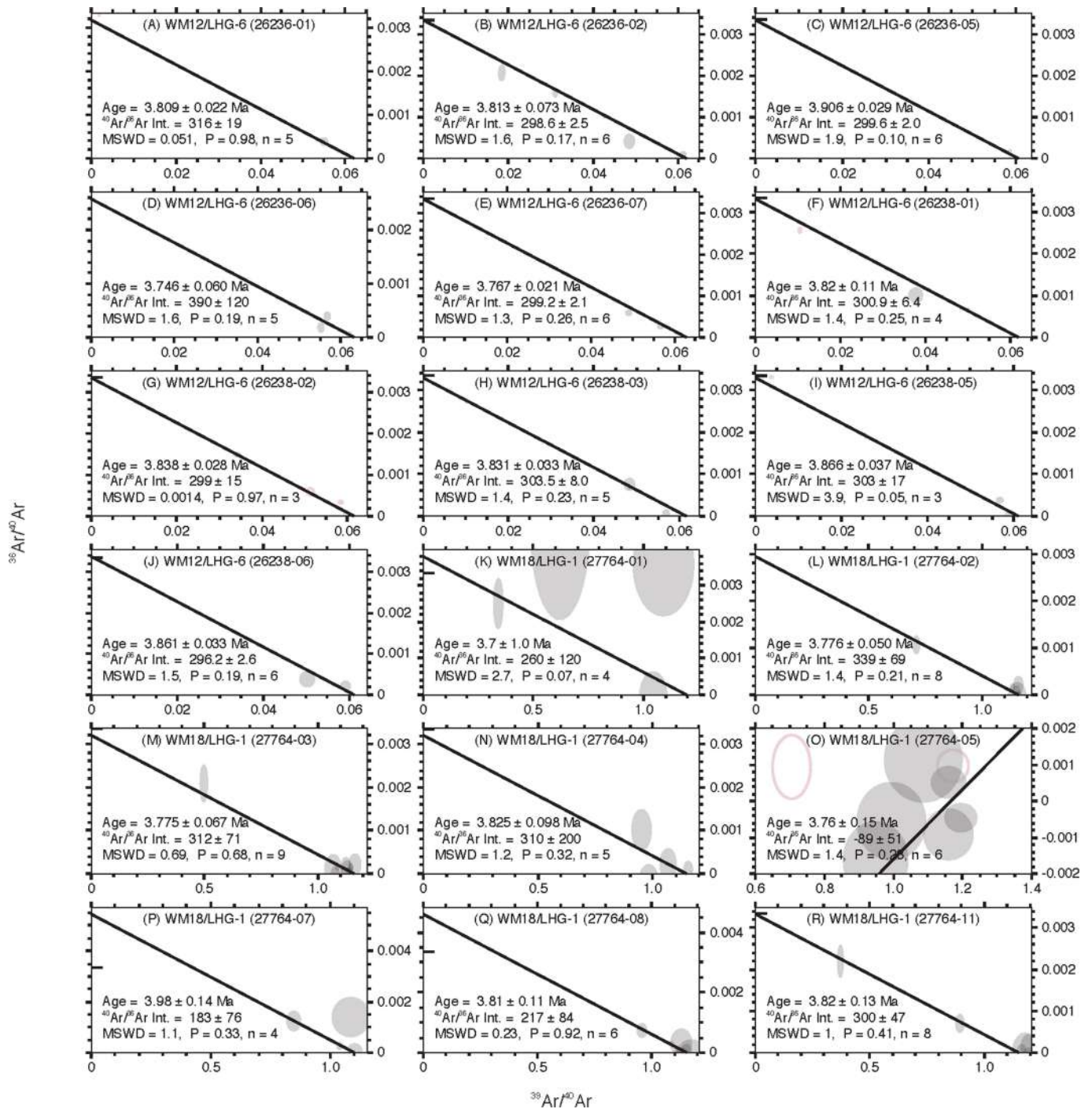
Extended Data Fig. 5 | Inverse-isochron correlation plots of plateau steps from incremental heating experiments. Plots show isotope correlation diagrams for $^{36}Ar/^{40}Ar$ and $^{39}Ar/^{40}Ar$ ratios Each grain is plotted separately. The age is obtained from the x-axis intercept and is shown with a 1σ modified standard error. '$^{40}Ar/^{39}Ar$ Int.' refers to the 'trapped' non-radiogenic $^{40}Ar/^{36}Ar$ ratio derived from the y-axis intercept

of the isochron. 'P' refers to the probability that the observed scatter can be explained by analytical errors alone; a value below 0.05 indicates that analytical errors are insufficient to explain the magnitude of the dispersion (that is, geological scatter is present). 'n' indicates the included number of analyses.
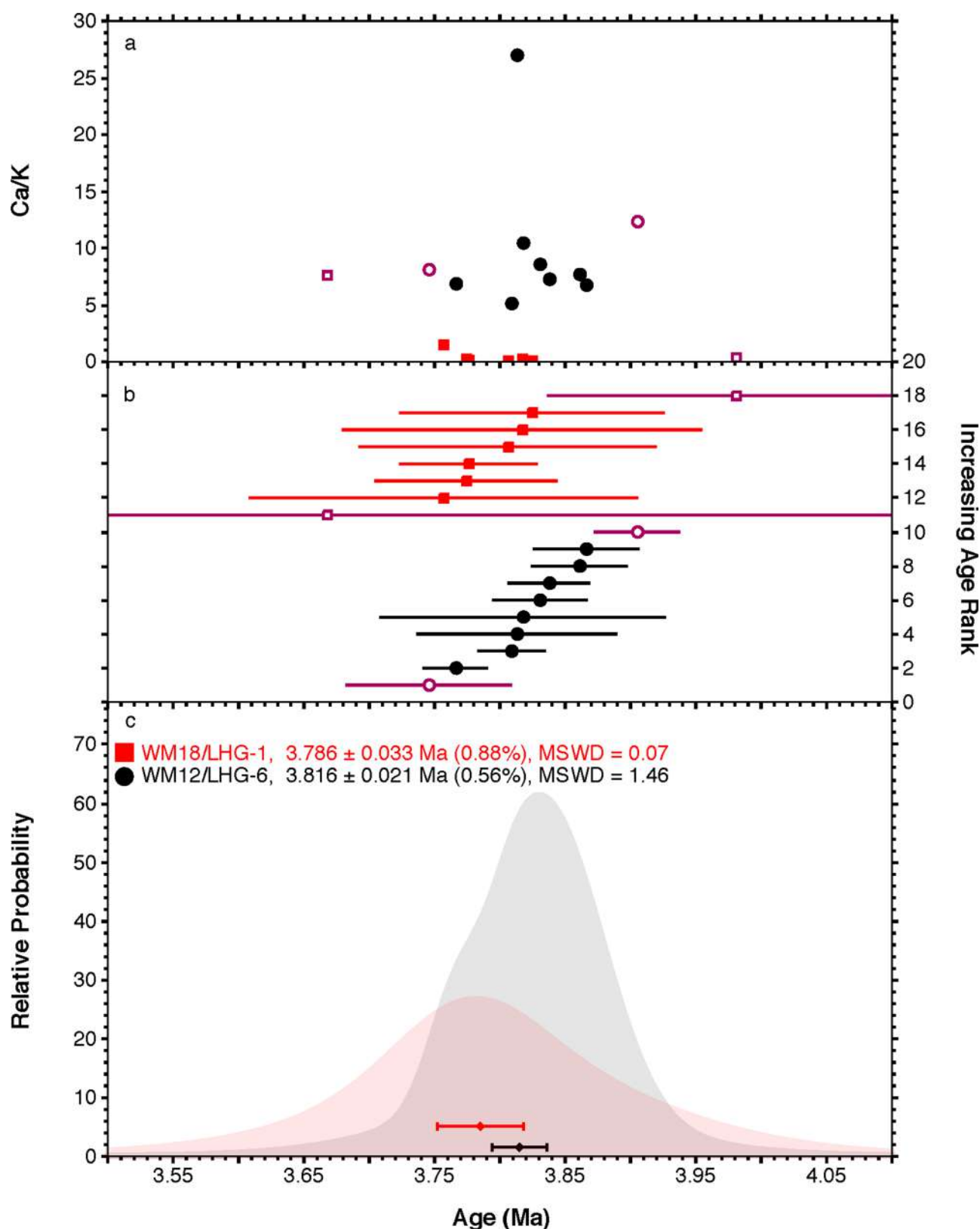
Extended Data Fig. 6 | Age-probability density plot of ages derived from isochron analyses. a, Mean Ca/K atomic ratio of individual grains estimated from $^{37}Ar/^{39}Ar$ measurements. **b**, Rank-order plot of single-crystal isochron results with 1σ analytical uncertainty. **c**, The vertical scale is the relative likelihood of a given age occurring in the sample. The weighted-mean ages of the population are shown, the 1σ error includes the error in *J*, the neutron-fluence parameter. The MSWD and number of included analyses are included after the mean age. Values in purple were omitted from analyses based on distance from the median age, with the cut-off level of 2.0 normalized median absolute deviations[46]. For sample WM12/LHG-6, eight out of ten isochron results are included in the weighted mean; for sample WM18/LHG-1, six out of eight results are included.
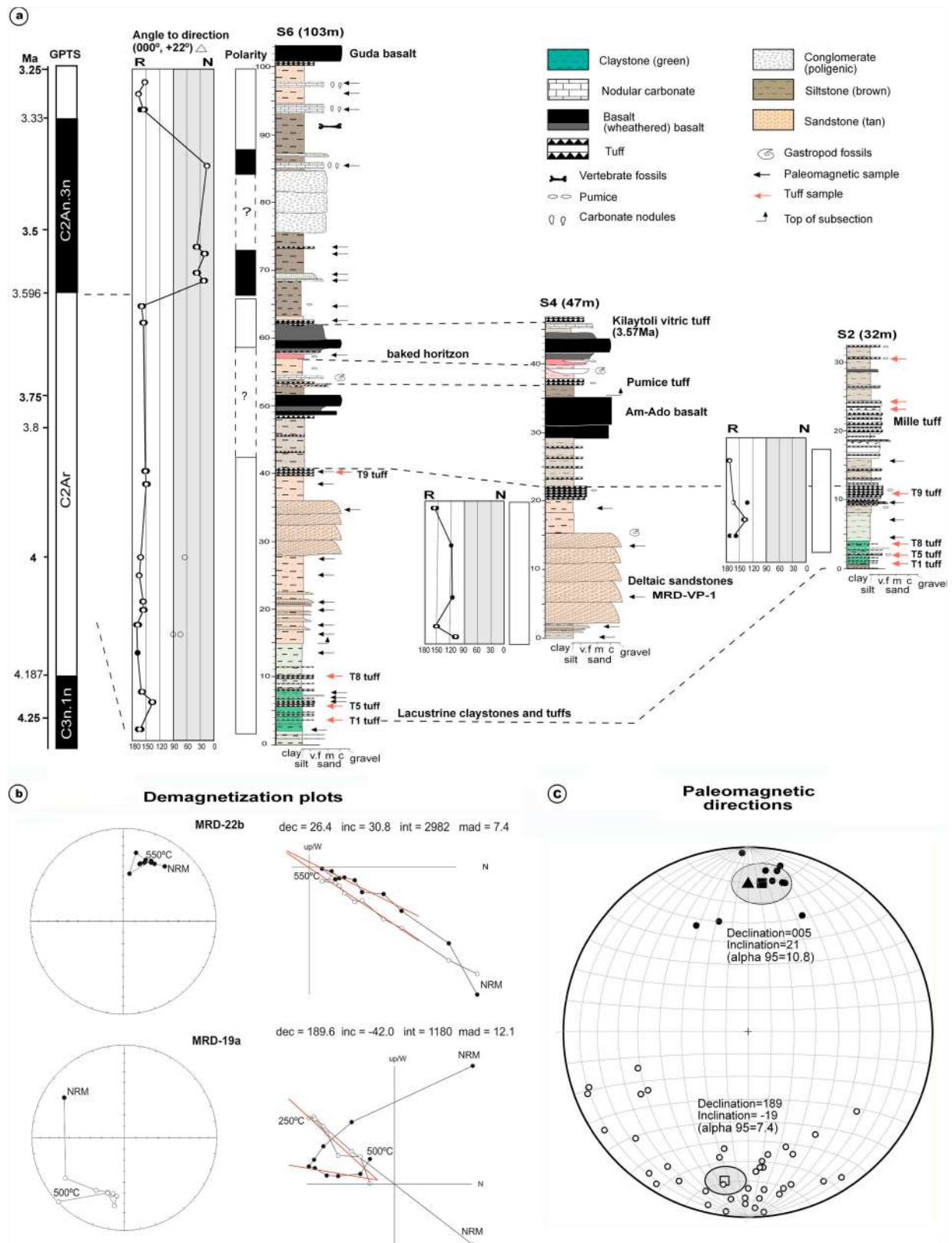
Extended Data Fig. 7 | See next page for caption.

Extended Data Fig. 7 | Palaeomagnetic results. a, Magnetostratigraphy for sections S6, S4 and S2 with results expressed as the angle to expected normal direction (Δ). The reverse–normal–reverse polarity sequence in S6 is correlated with the GPTS[24] on the basis of dated and geochemically identified tuffs in S2. White circles are mean directions of specimens (black), open circles are ambiguous specimen directions. vf, very fine sand; m, medium sand; C, coarse sand. **b**, Stereoplots and orthogonal demagnetization diagrams for a reverse (MRD-19a) and a normal (MRD-22b) sample. dec, declination; inc, inclination; int, intensity; NRM, natural remanent magnetization. The plots show the stepwise demagnetization process and the characteristic remanent magnetization directions (red lines) calculated using a principal component analysis[47]. In the stereonet plots (left), open circles show negative inclinations and solid dots show positive inclinations. In the orthogonal plots (right), solid dots indicate declination values and empty circles inclination values. Intensity units are in 10 A m^{-1}. mad, maximum angle deviation. **c**, Stereographic projection, referred to magnetic North of characteristic remanent magnetization directions for specimens collected at S6, S4 and S2. Circles indicate individual specimens. The plot shows the associated normal and reversed mean directions (squares) of the specimens, as determined by Fisher statistics, and the position of the present field (triangle). Only those samples showing non-ambiguous directions are plotted. In total, 48 specimens show reverse polarity and 10 samples show normal polarity.
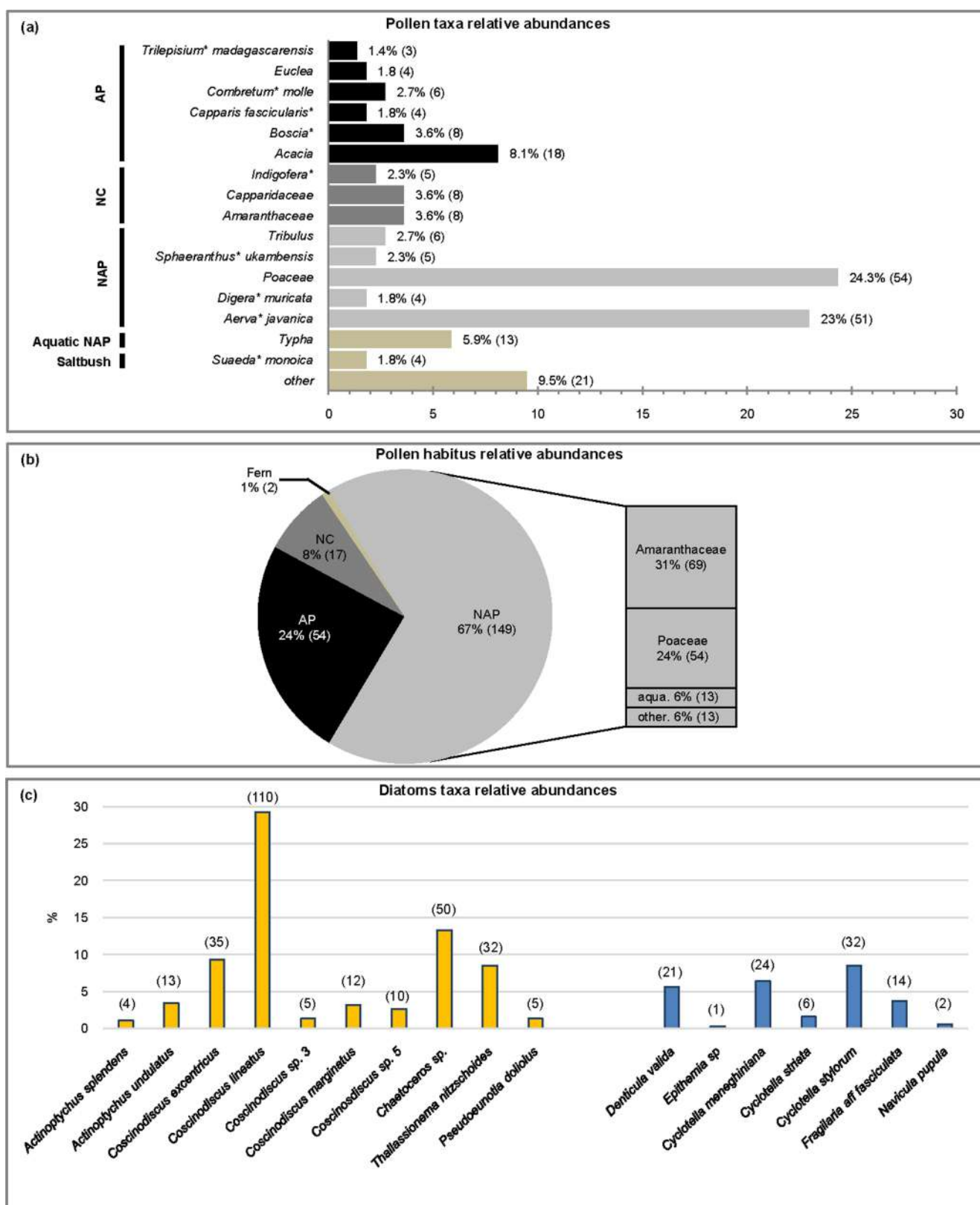
Extended Data Fig. 8 | Pollen diagrams for sample WM18-MRD-210 and diatom diagram for WM18-LHG-248. a, Relative abundances of pollen taxa (percentage) in WM18-MRD-210 calculated using the total number of pollen grains and fern spores. The asterisk indicate '-type'. Numbers in brackets refer to the number of pollen grains. **b**, Relative abundance of arboreal pollen (AP; trees and shrubs), non-arboreal pollen (NAP; herbs and forbs) and non-classified habitus (NC) in WM18-MRD-210. Numbers in brackets refer to the number of pollen grains. aqua., aquatic. **c**, Distribution of diatoms in WN18-LGH 248 according their ecological affinity: coastal–marine (yellow) versus brackish lacustrine (blue) environments. Among the species with coastal–marine affinities, *Coscinodiscus lineatus* and *Coscinodiscus excentricus* are typically observed in the Indian Ocean and Mozambique Channel[48,49]. Numbers in brackets refer to the number of diatom samples.
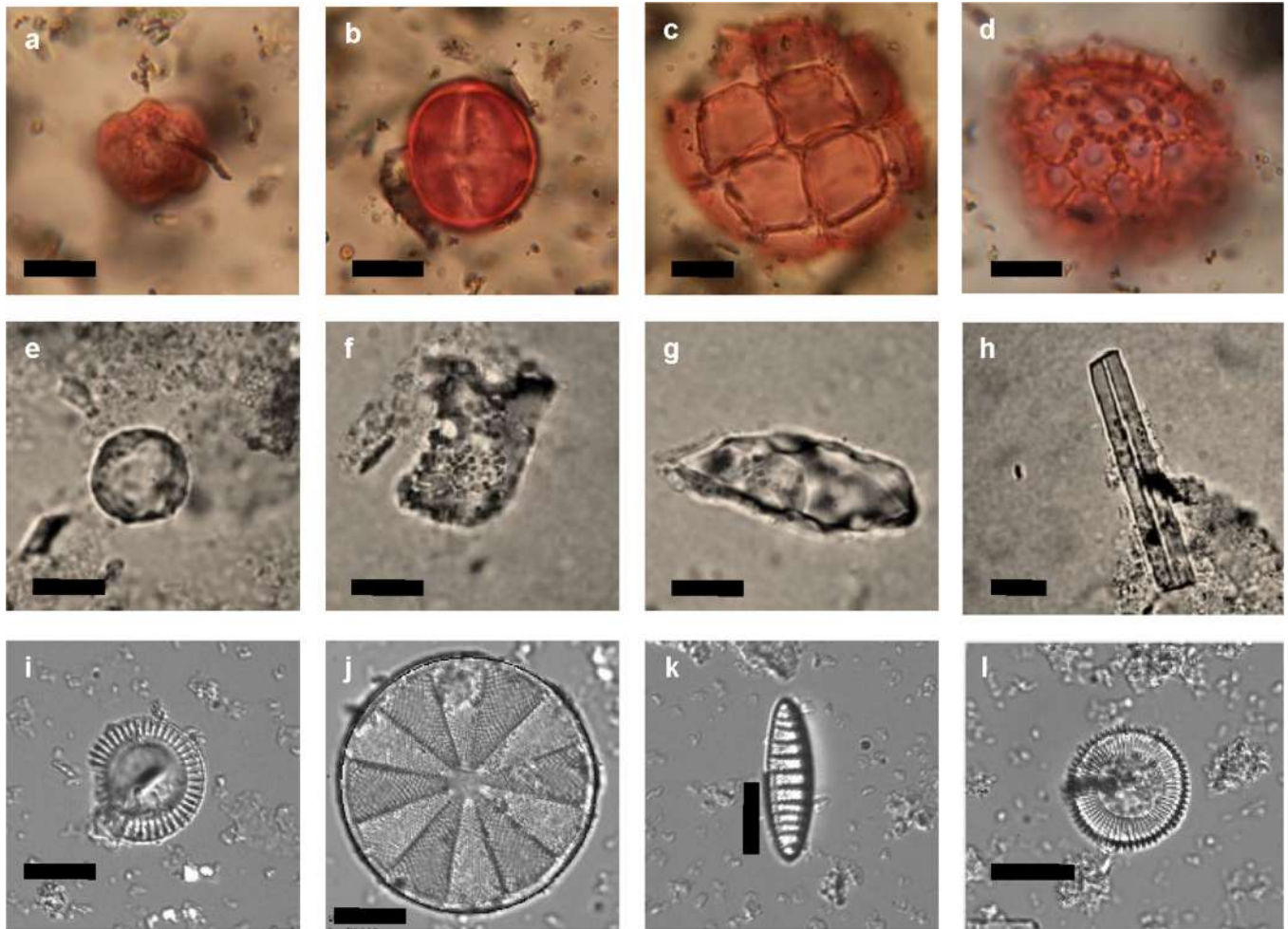
Extended Data Fig. 9 | Examples of fossil pollen grains (sample WM18-MRD-210) and biogenic silica remains (sample WM18-LHG-248). a–d, Pollen grains. **a**, *Aerva*-type *javanica*. **b**, *Euclea*. **c**, *Acacia*. **d**, *Tribulus*. **e–g**, Phytolith bodies. **e**, A spherical/globular psilate body, probably an indicator of dicot tree/shrub taxa. **f, g**, Two unidentified phytolith remains. **h**, A sponge spicule. **i–l**, Diatom frustules. **i**, *Cyclotella meneghiniana*. **j**, *Actinoptychus splendens*. **k**, *Denticula valida*. **l**, *Cyclotella stylorum*. Scale bars, 10 μm.
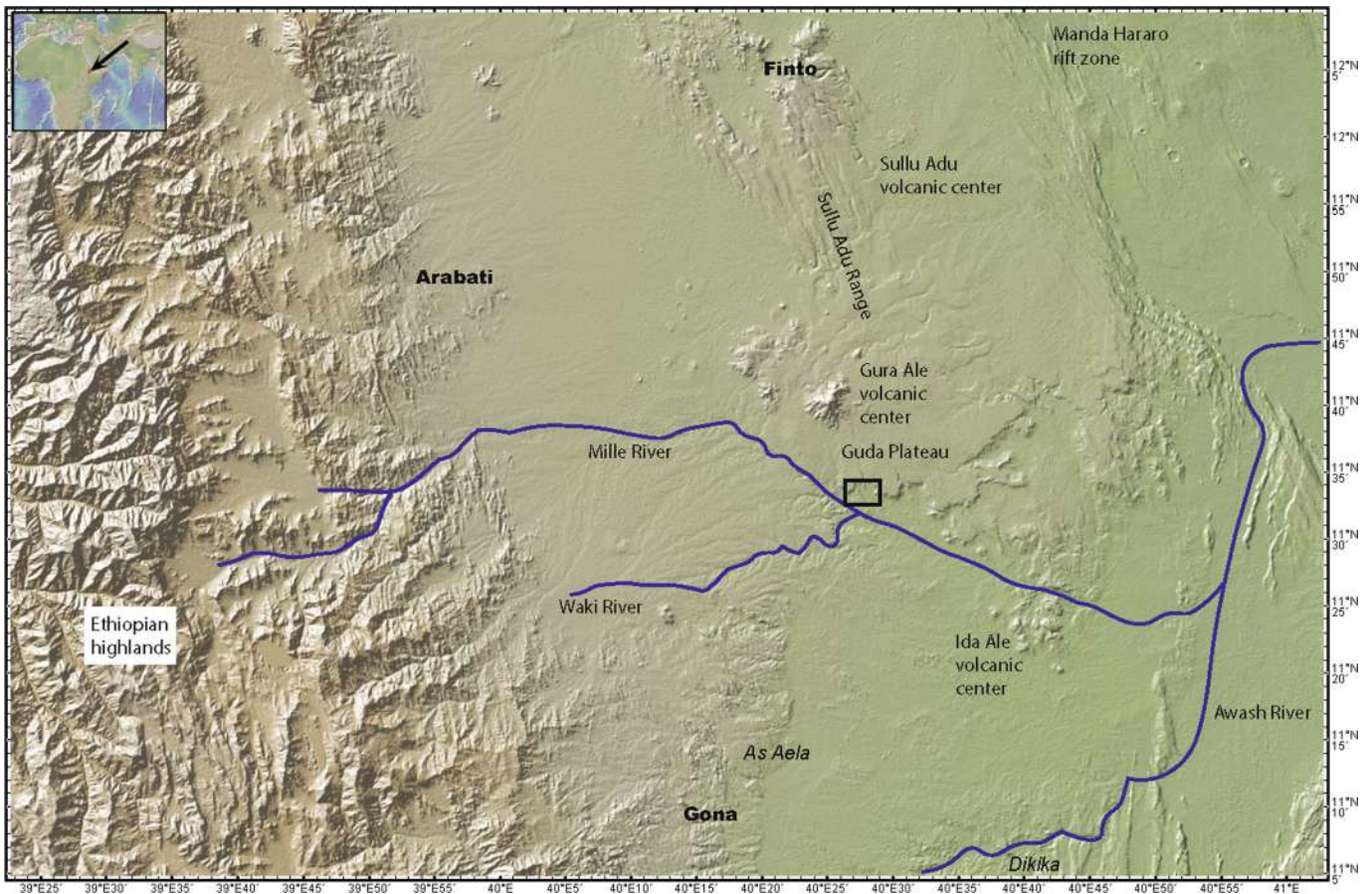
Extended Data Fig. 10 | Shaded relief of west central Afar. Volcanic and sedimentary strata of the Sullu Adu Range (including the Guda Plateau) are sub-horizontal, 4 Myr old and younger, and stratigraphically above Oligocene and Miocene basalts and rhyolites that are tilted to the east-northeast, indicating periods of extension[32] before approximately 4 Myr ago. Nearby areas with well-studied exposures[13,32] of these Oligocene and Miocene formations are labelled in bold. Areas with lake deposits[10,13] in the lower Hadar or upper Sagantole formations are labelled in italics. The base map is from http://www.geomapapp.org using the global multi-resolution topography synthesis[50].

nature research

Corresponding author(s):	Yohannes Haile Selassie
Last updated by author(s):	Jul 18, 2019

Reporting Summary

Nature Research wishes to improve the reproducibility of the work that we publish. This form provides structure for consistency and transparency in reporting. For further information on Nature Research policies, see Authors & Referees and the Editorial Policy Checklist.

Statistics

For all statistical analyses, confirm that the following items are present in the figure legend, table legend, main text, or Methods section.

n/a	Confirmed	
☐	☒	The exact sample size (n) for each experimental group/condition, given as a discrete number and unit of measurement
☐	☒	A statement on whether measurements were taken from distinct samples or whether the same sample was measured repeatedly
☐	☒	The statistical test(s) used AND whether they are one- or two-sided *Only common tests should be described solely by name; describe more complex techniques in the Methods section.*
☒	☐	A description of all covariates tested
☐	☒	A description of any assumptions or corrections, such as tests of normality and adjustment for multiple comparisons
☐	☒	A full description of the statistical parameters including central tendency (e.g. means) or other basic estimates (e.g. regression coefficient) AND variation (e.g. standard deviation) or associated estimates of uncertainty (e.g. confidence intervals)
☒	☐	For null hypothesis testing, the test statistic (e.g. F, t, r) with confidence intervals, effect sizes, degrees of freedom and P value noted *Give P values as exact values whenever suitable.*
☐	☒	For Bayesian analysis, information on the choice of priors and Markov chain Monte Carlo settings
☒	☐	For hierarchical and complex designs, identification of the appropriate level for tests and full reporting of outcomes
☒	☐	Estimates of effect sizes (e.g. Cohen's d, Pearson's r), indicating how they were calculated

Our web collection on statistics for biologists contains articles on many of the points above.

Software and code

Policy information about availability of computer code

Data collection	MSD ChemStation D.01.02.16 15-JUNE-2004 ISODAT 3.0 Probe for EPMA version 10.0.4
Data analysis	Excel version 15.23.2, Paldir version 5.5 software for paleomagnetic demagnetization diagrams (Utrecht University); Stereonet version 9.6 (R.W. Allmendinger, Cormell University); R software version 3.5.1 for biome calculations from pollen data; Probe for EPMA version 10.0.4 for analysis of EPMA data on glass composition, Bayesian stratigraphic code (https://github.com/brenhinkeller, Keller, 2018); a data analysis version of the 40Ar/39Ar dating software is available at no cost from adeino@bgc.org

For manuscripts utilizing custom algorithms or software that are central to the research but not yet described in published literature, software must be made available to editors/reviewers. We strongly encourage code deposition in a community repository (e.g. GitHub). See the Nature Research guidelines for submitting code & software for further information.

Data

Policy information about availability of data

All manuscripts must include a data availability statement. This statement should provide the following information, where applicable:

- Accession codes, unique identifiers, or web links for publicly available datasets
- A list of figures that have associated raw data
- A description of any restrictions on data availability

Correspondence and requests for material should be addressed to yhaileselassie@cmnh.org. Data are available as tables in Supplementary Information. Associated raw data: Figure 1 - Table 1,2,3,4; Figure 2; Table 2,3,4,6,8,9,10; Ext Dat Fig 1 - Table 1; Ext Dat Fig 2 - Table 2, 5; Ext Dat Fig 3 - Table 4,6,7,8,9; Ext Dat Fig 4,5,6 - Table 3; Ext Dat Fig 7 - Table 4; Ext Dat Fig 8 Table 9, 10. Any data that support the findings of this study, but are not included in the Supplementary Information, are available from the corresponding authors upon reasonable request.

Field-specific reporting

Please select the one below that is the best fit for your research. If you are not sure, read the appropriate sections before making your selection.

☐ Life sciences   ☐ Behavioural & social sciences   ☒ Ecological, evolutionary & environmental sciences

For a reference copy of the document with all sections, see nature.com/documents/nr-reporting-summary-flat.pdf

Ecological, evolutionary & environmental sciences study design

All studies must disclose on these points even when the disclosure is negative.

Study description	Area around fossil discovery site in the Godaya River Valley of the Woranso Mille project area, Ethiopia.
Research sample	Samples of basalt, volcanic tuff, sediment from the study area plus all identifiable mammalian vertebrate fossils from MRD-VP-1.
Sampling strategy	Tuff and sediment samples were collected from measured stratigraphic sections and basalt samples from across the study area.
Data collection	Basalt samples were collected by M. Alene and recorded by him. Tuff samples were collected by B. Saylor for tephrochemistry and A. Deino for Ar/Ar dating and recorded by them. Sediment samples were collected by L. Gibert for paleomagnetic work. N. Levin and Mark Peaple collected sediment samples for analysis of botanical remains. Y. Haile-Selassie directed the project and the collection of vertebrate fossils with assistance from S. Melillo.
Timing and spatial scale	Samples were collected over multiple field seasons, starting in 2011, with a push during 2017. Sampling focused on well exposed sections near the fossil site.
Data exclusions	Tephra geochemistry: Analyses with totals less than 97.5 or greater than 102.5 were excluded except for MRD-17-4 for which analyses with water adjusted totals less than 89.5 were excluded. Ar/Ar dating: In the case of WM18/LHG-1, each grain was analyzed in one or two low-power steps to allow a preliminary assessment of age and chemistry; grains that were too old (>10 Ma, n=12) or exhibited a Ca/K ratio of plagioclase (n=1) were omitted, leaving eight grains taken to completion of the incremental heating sequence. For the calculation of the age-probability density plot omitted analyses based were based on distance from the median age, with the cutoff level of 2.0 'normalized median absolute deviations'46.For sample WM12/LHG-6, n=8 out of 10 isochron results are included in the weighted mean; for sample WM18/LHG-1, n=6 out of 8 results are included. Plant wax: 16 samples were analyzed for plant wax biomarkers, one sample yielded biomarker concentrations too low for isotopic analyses.
Reproducibility	Paleomagnetic measurements: At least two specimens from each sample (total of 79 specimens) were thermally demagnetized in a non-inductive furnace (<10 nT), at 50ºC steps up to 650ºC to remove secondary magnetizations and to isolate the primary characteristic magnetic direction. Plant wax carbon and hydrogen isotopic analyses were replicated at target responses of 2.5-6 V and 3-6 V respectively; replicates outside of the dynamic range set by the prior linearity tests were excluded; all attempts at replicate measurement in that range were successful. Basalt geochemistry: Table 1: Chemical error based on replicate analyses of BHVO-2, a United States Geological Survey Geochemical Standard
Randomization	This is not relevant for our study because samples were analyzed individually and not assigned to groups.
Blinding	Blinding was not relevant to this study because it was a field study not an experimental study.

Did the study involve field work?   ☒ Yes   ☐ No

Field work, collection and transport

Field conditions	Arid, limited tree cover, low relief river valley between high, basalt covered plateaus, and hot.
Location	Area around fossil discovery site in the Godaya River Valley of the Woranso Mille project area, Afar Region, Ethiopia (11º32'59.5" N; 40º27'54.6" E)
Access and import/export	Access and sample export followed the laws and regulations of Ethiopia and the Afar state, with permission from the Authority for Research and Conservation of Cultural Heritage (ARCCH) of the Ministry of Culture and Tourism of Ethiopia, dated November 17, 2015 (Ref. # 08/KT-69/005), allowed us to conduct field research that led to the discovery of the subject of this manuscript, collect geological samples, and export them for further analysis.
Disturbance	Camping, road access, and sample collection provided minimal disturbance.

Reporting for specific materials, systems and methods

We require information from authors about some types of materials, experimental systems and methods used in many studies. Here, indicate whether each material, system or method listed is relevant to your study. If you are not sure if a list item applies to your research, read the appropriate section before selecting a response.

Materials & experimental systems

n/a	Involved in the study
☒	☐ Antibodies
☒	☐ Eukaryotic cell lines
☐	☒ Palaeontology
☒	☐ Animals and other organisms
☒	☐ Human research participants
☒	☐ Clinical data

Methods

n/a	Involved in the study
☒	☐ ChIP-seq
☒	☐ Flow cytometry
☒	☐ MRI-based neuroimaging

Palaeontology

Specimen provenance	Samples were collected with permits from the Authority for Research and Conservation of Cultural Heritage of Ethiopia. Field work at the site is conducted with permits from the Authority for Research and Conservation of Cultural Heritage of the Ministry of Culture and Tourism of Ethiopia issued on November 17, 2015, Ref. # 08/KT-69/005.
Specimen deposition	Fossil specimens are deposited in the Paleoanthropology Laboratory of the National Museum of Ethiopia
Dating methods	40Ar/39Ar laser incremental heating dating of single crystal phenocrysts in felsic volcanic tuffs. 40Ar/39Ar dating was conducted at the Berkeley Geochronology Center (BGC) in Berkeley, California, USA.

☒ Tick this box to confirm that the raw and calibrated dates are available in the paper or in Supplementary Information.